# Application of cyclometalated rhodium(III) complexes as therapeutic agents in biomedical and luminescent cellular imaging

Marzieh Sohrabi [a,1], Maryam Bikhof Torbati [b,2,*], Martin Lutz [c,*], Soraia Meghdadi [a,3], Hossein Farrokhpour [a,4], Ahmad Amiri [d,5], Mehdi Amirnasr [a,6,*]

[a] *Department of Chemistry, Isfahan University of Technology, Isfahan 8415683111, Iran*
[b] *Department of Biology, Yadegar-e-Imam Khomeini (RAH) Shahr-e-Rey Branch, Islamic Azad University, Tehran, Iran*
[c] *Crystal and Structural Chemistry, Bijvoet Centre for Biomolecular Research, Faculty of Science, Utrecht University, Padualaan 8, 3584 CH Utrecht, the Netherlands*
[d] *Department of Chemistry, College of Science, University of Tehran, Tehran 14155-6455, Iran*

## ARTICLE INFO

## ABSTRACT

The synthesis and characterization of three [Rh(ppy)$_2$(N˄N)][PF$_6$] complexes, [Rh(ppy)$_2$(pybtz)][PF$_6$].CH$_3$OH (**Rh1**), [Rh(ppy)$_2$(pzbtz)][PF$_6$] (**Rh2**) and [Rh(ppy)$_2$(qbtz)][PF$_6$] (**Rh3**) [Hppy: 2-phenylpyridine; N˄N: (pyridin-2-yl)benzo[d]thiazole (**pybtz**), (pyrazin-2-yl)benzo[d]thiazole (**pzbtz**), and (quinolin-2-yl)benzo[d]thiazole (**qbtz**)], and single crystal structures of **Rh1** and **Rh3** are reported. **Rh1** and **Rh3** show high fluorescent intensities upon excitation at 400 and 410 nm, respectively. Evaluation of lipophilicity by theoretical calculations indicates **Rh3** > **Rh1** > **Rh2**, introducing **Rh3** as the best candidate for biological studies. The **Rh3** exhibits anticancer activity, with high cellular uptake efficiency and good cytotoxicity against MCF-7 cell line as compared to the non-malignant MRC-5 cells. Flow cytometry have confirmed the apoptosis cell death and cell cycle arrest in the sub-G1 phase. The result of real time PCR shows that **Rh3** induces apoptosis by up-regulating of *p53*, miR-15a, miR-16–1 and miR-29b and down regulating of *bcl-2* and miR-21 at the level of RNA transcription. Importantly, cell imaging experiments have demonstrated that **Rh3** can be considered as a new promising metallodrug candidate for cancer treatment.

## 1. Introduction

Small organic molecules have demonstrated to be drug candidates and invaluable tools for studying biological systems. In this context benzothiazole and its derivatives have attracted considerable attention because of their wide range of pharmacological activities. Moreover, their potency in cancer therapy has become an area of particular interest in recent years [1]. Compared with organic small molecule-based drugs, metal complexes can display unique and specific geometries and tunable reactivities [2–7]. These complexes with such advantages play an important role in cancer drug research. While ruthenium, palladium, and platinum complexes as metallodrugs have contributed tremendous advances in the field of inorganic medicinal chemistry over the past few decades [4–7], recently, organometallic compounds, with properties somewhat intermediate between classical inorganic and organic drugs, have become the focus of attention in the realm of therapeutic. Among

these organometallic compounds, complexes of group 9 metals specially rhodium and iridium, have attracted recent interest due to their tunable reactivity (from kinetically liable to substitutionally inert), remarkable water solubility, air and moisture-stability, and relatively facile synthesis. Moreover, the role of small drug-like heterocyclic compounds, as chelating ancillary ligands for the synthesis of rhodium and iridium organometallic complexes, have been very well recognized for biomedical applications in cancer cell killing and cell imaging [8–12]. While the rhodium(III) centre has been traditionally regarded as kinetically inert, it has recently been documented that its reactivity toward biological targets can be adjusted by coordinating appropriate ligands [12,13].

In addition to the therapeutic applications, group 9 heavy-metal complexes showing room temperature phosphorescent emission [14–21], are the most widely used compounds in luminescent bioimaging, especially for the imaging of living cells. Compared with small-organic molecules, photoluminescent heavy-metal complexes of group 9 elements offer unique advantages in bioimaging applications, such as (i) high emission quantum yield (ii) significant separation between absorption and emission maximua (often > 5000 cm$^{-1}$) for easily distinguishing emission over excitation, and minimizing fluorescence reabsorption (iii) relatively long phosphorescence lifetime (hundreds of nanoseconds to tens of microseconds), that can be utilized for filtering auto-fluorescence from biological samples by time-resolved luminescence imaging and time-gated luminescence imaging technology [22]. Moreover, the emission properties of these metal complexes can be readily tuned, by using a variety of ligands of different structural, electronic, and coordinating properties [23]. These complexes exhibit high photostability and provide promising platforms for continuous monitoring of biological events by fluorescence spectroscopy and microscopy [22]. Besides, the cytotoxicity of luminescent heavy-metal complexes depends strongly on their chemical structures, and can be correlated with their lipophilicity. Usually, the complexes with high lipophilicity exhibit good membrane permeability and are highly cytotoxic [24,25].

Among group 9 elements, the monocationic iridium(III) complexes with two cyclometalated ligands such as phenylpyridine (ppy) or its derivatives and a diimine ancillary ligands such as bipyridine (bpy), [Ir(ppy)$_2$(N^N)]$^+$, are the most usual form of Ir complexes that act as imaging agents [24–31]. Interestingly, functionalization of nanoparticle surfaces with bioimaging agents such as Ru (II) and Ir (III) complexes have been used in combined therapies with synergistic effects and in bioimaging [32–34]. The very few Rh(III) complexes reported in imaging are of analogous coordination features. It has been documented that Rhodium(III) complexes rarely display strong phosphorescence at room temperature [10]. In this context several research groups have investigated the photophysical properties of [Rh(C^N)$_2$(N^N)]$^+$ complexes containing diimines or their derivatives as the (N^N) ancillary ligands [10,35–37]. To the best of our knowledge, no cyclometalated [Rh(C^N)$_2$(N^N)]$^+$ complex with benzothiazole moiety as part of the ancillary N^N ligand has been reported. Moreover, there are only a few reports on [Ir(C^N)$_2$(N^N)]$^+$ complexes with benzothiazole derivatives as

the N^N ligand. Examples are, the iridium(III) complex of (N^N = 2-(pyridin-2-yl)-4,5-dihydrothiazole) with potential application as a photosensitizer for catalytic water reduction [38], and iridium(III) complexes of (N^N = 2-(Pyridin-2-yl)benzo[d]thiazole) and its derivatives for the fabrication of extremely stable red-emitting LECs [39].

On the basis of the promising potential of rhodium complexes as medicinal and bioimaging agents, herein, we report the efficient synthesis of three novel luminescent cationic benzothiazole Rh(III) cyclometalated complexes with a general structure of [Rh(C^N)$_2$(N^N)]$^+$ by altering the ancillary N^N ligand (C^N = 2-phenyl-pyridine; N^N = **pybtz**, **pzbtz**, and **qbtz**), Scheme 1.

Among the three complexes [Rh(C^N)$_2$(pybtz)]PF$_6$ (**Rh1**), [Rh(C^N)$_2$(pzbtz)]PF$_6$ (**Rh2**), and [Rh(C^N)$_2$(qbtz)]PF$_6$ (**Rh3**), **Rh1** and **Rh3** show remarkable absorption /emission efficiency. The cationic character of these complexes contributes to more efficient cell membrane permeability. Considering the calculated lipophilicity order of **Rh3** > **Rh1** > **Rh2**, complex **Rh3**, with the highest lipophilicity, is selected for biological studies. Interestingly, the lipophilicity, and cell uptake rates of complex **Rh3** is enhanced relative to its ancillary ligand, **qbtz**. This complex shows anticancer activity, with the high cellular uptake efficiency and acceptable cytotoxicity against MCF-7 cancer cell line relative to the non-malignant MRC-5 cell line. The capability of this complex in cell apoptosis induction, cell cycle arrest, modification of the expression level of several apoptotic pathway genes, and cell imaging are also studied and discussed.

## 2. Experimental section

### 2.1. Materials and methods

All solvents, chemicals and biological reagents were commercially available and purchased from Aldrich and Merck, Gibco, and Cinnagen, and used without further purification. UV–vis spectra were measured on a JASCO V-570 spectrophotometer. Photoluminescence spectra were recorded on a RF-5301PC Shimadzu fluorescence spectrofluorophotometer. Infrared spectra were recorded on a FT-IR JASCO 680 plus spectrophotometer as KBr pellet. Elemental analyses were carried out using a Perkin–Elmer 2400II CHN elemental analyzer. $^1$H NMR spectra were obtained on a Bruker AVANCE III 300 spectrometer. Proton chemical shifts are reported in ppm relative to an internal standard of Me$_4$Si. Electrochemical measurements were recorded using a SAMA 500 Research Analyzer. Flow cytometry was performed by an Annexin V/PI model VD-Facscalibur flow cytometer. Quantitative real-time PCR (qRT-PCR) was performed on Exicycler 96 bioneer. Cell images were captured with a Leica TCS SPE (Zeiss) laser scanning confocal microscope.

### 2.2. Synthetic protocols and characterization

The precursor complex, cyclometalated Rh(III) μ-chloro-bridged dimer [Rh(ppy)$_2$Cl]$_2$, was synthesized by heating RhCl$_3$·3H$_2$O with 2.5 equiv. of the cyclometalating ligand, Hppy, in glycerol [40]. The purity of the product was confirmed by elemental analysis.
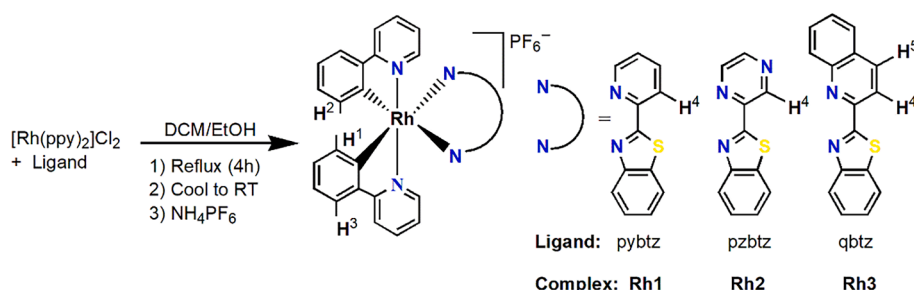


**Scheme 1.** Synthesis of cyclometalated rhodium(III) complexes **Rh1**-**Rh3**, with benzothiazole ligands.

### 2.2.1. Synthesis of the three ancillary $N^\wedge N$ Ligands.

The **pybtz** and **qbtz** ligands were prepared according to a procedure reported elsewhere [41]. This procedure was also used for the synthesis of the new ligand **pzbtz**. The synthetic approach was initiated using a mixture of 2-pyrazinecarboxylic acid (5 mmol, 0.621 g) and 2-amino-thiophenol (5 mmol, 0.626 g) with triphenylphosphite (5 mmol, 1.551 g) in the presence of the inexpensive ionic liquid tetrabuty-lammonium bromide (TBAB) (5 mmol, 1.612 g) at 120 °C. The reaction was completed in 15 min. The final viscous slurry was cooled to room temperature and then treated with cold methanol. The resulting solid was filtered off, washed with cold methanol and dried under vacuum.

Yield: 0.874 g (82%). Anal. Calcd. for $C_{11}H_7N_3S$ (213.26): C, 61.95; H, 3.31; N, 19.70%. Found: C, 61.27; H, 3.23; N, 19.28%. FT–IR (KBr, $cm^{-1}$): 3054, 1591, 1550, 1509, 1489, 1456, 1432, 1402. UV–vis: $\lambda_{max}$ (nm) ($\varepsilon$, L $mol^{-1}$ $cm^{-1}$) (DMSO-$H_2O$, 1:1 v/v): 342 sh (11940), 322 (16370), 274 (14850). $^1H$ NMR (300 MHz, $CDCl_3$) $\delta$ (ppm) = 9.61 (d, $^3J$ = 1.35 Hz, 1H), 8.66 (d, $^3J$ = 2.52 Hz, 1H), 8.64 (d, $^3J$ = 1.47 Hz, $H_f$), 8.14 (d, $^3J$ = 8.29 Hz, $H_d$), 7.97 (d, $^3J$ = 7.61 Hz, $H_a$), 7.54 (t, $^3J$ = 9 Hz, $^3J'$ = 1 Hz, 1H), 7.45 (t, $^3J$ = 7.5 Hz, $^3J'$ = 1 Hz, 1H).

### 2.2.2. Synthesis of Rhodium(III) Complexes.

General Procedure. A mixture of $[Rh(ppy)_2Cl]_2$ complex (0.089 g, 0.1 mmol) and the benzothiazole ligand (**pybtz, pzbtz, qbtz**) (0.25 mmol) in 15 mL ethanol-dichloromethane solution (2:1 v/v) were refluxed for 4 h. The volume of the resulting yellow solution was then reduced to 1.5 mL by evaporation at room temperature, and 2 mL of water was then added to the residue. The complex was subsequently precipitated by adding excess aqueous $NH_4PF_6$ to the solution. After filtration the crude product was recrystallized from a mixture of suitable solvents.

$[Rh(ppy)_2pybtz]PF_6$. (**Rh1**). Solvent of recrystallization: $CH_2Cl_2$/MeOH (2:1 v/v). Yield: 1.614 g (84%). Anal. Calcd. for $RhC_{34}H_{24}N_4F_6SP$ (768.52): C, 53.14; H, 3.15; N, 7.29%. Found: C, 53.61; H, 3.14; N, 7.34%. FT–IR (KBr, $cm^{-1}$): 3596, 3054, 1606, 1580, 1560, 1482, 1438,1420, 839, 757. UV–vis: $\lambda_{max}$ (nm) ($\varepsilon$, L $mol^{-1}$ $cm^{-1}$) (DMSO-$H_2O$, 1:1 v/v): 264 (62760), 316 (26710), 336 (22510), 372 (8080), 420 (193). $^1H$ NMR (300 MHz, DMSO-$d_6$) $\delta$ (ppm) = 8.71 (bd, $^3J$ = 7.88 Hz, 1H), 6.96–8.37 (m, 20H), 6.75 (bd, $^3J$ = 8.34 Hz, 1H), 6.29 (bd, $^3J$ = 7.62 Hz, 1H), 6.17 (bd, $^3J$ = 7.63 Hz, 1H).

$[Rh(ppy)_2pzbtz]PF_6$. (**Rh2**). Solvent of recrystallization: Acetone/EtOH (1:1 v/v). Yield: 1.558 g (81%). Anal. Calcd. for $RhC_{33}H_{23}N_5F_6SP$ (769.50): C, 51.51; H, 3.01; N, 9.10%. Found: C, 51.40; H, 2.98; N, 9.17%. FT–IR (KBr, $cm^{-1}$): 3063, 1606, 1579, 1548, 1481, 1438, 1422,1384, 844, 758. UV–vis: $\lambda_{max}$ (nm) ($\varepsilon$, L $mol^{-1}$ $cm^{-1}$) (DMSO-$H_2O$, 1:1 v/v): 264 (60340), 314 (22920), 346 (19550) 454 (261). $^1H$ NMR (300 MHz, DMSO-$d_6$) $\delta$ (ppm) = 8.97 (bd, $^3J$ = 2.70 Hz, 1H), 8.84–6.97 (m, 19H), 6.76 (bd, $^3J$ = 8.10 Hz, 1H), 6.24 (bd, $^3J$ = 7.50 Hz, 1H), 6.14 (bd, $^3J$ = 7.80 Hz, 1H).

$[Rh(ppy)_2qbtz]PF_6$. (**Rh3**). Solvent of recrystallization: $CH_2Cl_2$/EtOH (2:1 v/v). Yield: 1.678 g (82%). Anal. Calcd. for $RhC_{38}H_{26}N_4F_6SP$ (818.58): C, 55.76; H, 3.20; N, 6.84%. Found: C, 56.33; H, 3.16; N, 6.92%. FT–IR (KBr, $cm^{-1}$): 3101, 3051, 1603, 1581, 1555, 1517, 1480, 1437, 842, 760. UV–vis: $\lambda_{max}$ (nm) ($\varepsilon$, L $mol^{-1}$ $cm^{-1}$) (DMSO-$H_2O$, 1:1 v/v): 260 (95380), 320 (30720), 339 (32610), 354 (33750), 378 (12480), 448 (394). $^1H$ NMR (400 MHz, $CDCl_3$)

$\delta$ (ppm) = 8.79 (bd, $^3J$ = 8.40 Hz, 1H), 8.59 (bd, $^3J$ = 8.40 Hz, 1H), 8.10–7.02 (m, 21H), 6.75 (bd, $^3J$ = 8.34 Hz, 1H), 6.29 (bd, $^3J$ = 7.62 Hz, 1H), 6.17 (bd, $^3J$ = 7.63 Hz, 1H).

### 2.3. Electrochemical measurements

Cyclic voltammograms were recorded using a SAMA 500 Research Analyser. All measurements were carried out in a one-compartment cell under Ar gas, equipped with a glassy-carbon working electrode, a platinum disk auxiliary electrode, and Ag wire as a reference electrode. The glassy carbon working electrode (Metrohm 6.1204.110) with a 2.0 ± 0.1 mm diameter was manually cleaned with 1 μm alumina polish prior to each scan. Tetrabutylammonium hexafluorophosphate (TBAH) was used as the supporting electrolyte. The solutions were deoxygenated by purging with Ar for 5 min. All electrochemical potentials were calibrated versus an internal $Fc^+$/0 ($E = 0.40$ V vs. SCE) couple under the same conditions [42]. The scan rate was 50 mV $s^{-1}$.

### 2.4. Theoretical calculations

The entire calculations were performed using Gaussian 09 quantum chemistry package [43]. The molecular geometries of the **qbtz** ligand and the three rhodium complexes were fully optimized using DFT method employing M06L functional. All the DFT calculations were carried out in 1-octanol and water using the relativistic effective core pseudo potential LANL2DZ for the Rh atom and the 6–31 + G(d) basis set for C, H, N and S atoms. In order to calculate the log $P_{o/w}$ values and evaluate the lipophilicity of the **qbtz** ligand and Rh complexes, calculations of $\Delta G_{solv}$ were performed in 1-octanol and water solutions at the same functional and basis set. For two relatively immiscible solvents log $P_{o/w}$ can be considered proportional to the molar Gibbs free energy of transfer between 1-octanol and water [44]. This approach can be described using equation (1), where $\Delta G_w$ and $\Delta G_o$ are the solvation free energies of the solute in water and 1-octanol [45]. The polarized continuum model (PCM) was used for modelling the solvent in the calculations which considers only the electrostatic field of the solvent on the solute. The frequency calculations were performed on all optimized structures in the ground and selected excited electronic states to confirm that the optimized structures are in local minima.

$$-2.303\ RT\ \log P = \Delta G_{solv(1-octanol)} - \Delta G_{solv(water)} = \Delta G_{ow} \qquad (1)$$

### 2.5. Human cell culture

The human breast adenocarcinoma (MCF-7) cell line and normal human fibroblast cell line (MRC-5) were purchased from the National Cell Bank of Pasteur Institute of Iran. Cells were cultured in high glucose DMEM growth medium supplemented with 10% heat inactivated FBS (fetal bovine serum), 2 mM L-glutamine (Gibco BRL, Scotland) and 1% penicillin/streptomycin (100 U/mL penicillin and 100 μg/mL strepto-mycin) (Sigma, USA). Upon reaching 80% confluence, the cells were trypsinized (using 0.05% trypsin solution) and transferred into a new cell culture plate. Cells were incubated at 37 °C in a humidified 5% $CO_2$ during the entire culturing procedure.

### 2.6. Cell viability assay

We used MTT assay to survey the cytotoxic effect of the **qbtz** ligand and its complex (**Rh3**) toward MCF-7 and MRC-5 cells. 24 h prior to **qbtz** ligand and complex (**Rh3**) addition, MCF-7 (2500 cells/mL) and MRC-5 (2500 cells/mL) cells were separately plated in 96-well flat-bottom microtiter and 96-well microtiter plates. These compounds were then added at the desired concentrations (final concentration per well: 2, 4, 8, 16, and 32 μg/mL). Upon 24, 48 and 72 h of cell exposure to the compounds, *in vitro* cytotoxicity was determined by MTT (3-(-4,5-dime-thylthiazol-2-yl)-2,5-diphenyltetrazolium bromide) assay (Sigma Aldrich M2128). In brief, 20 μL MTT (5 μg/mL) solution was added to each well. After 4 h incubation, the supernatant was removed and each well was treated with DMSO (150 μL) for 15 min in order to dissolve the dye. Cell viability of each well/condition was quantified by measuring the absorbance at 570 nm on a plate reader (TECAN-Sunrise, Man-nedorf, Switzerland). All the values were normalized against the blank condition (control: cell culture growth medium) using equation (2):

$$\text{Cell viability (\%)} = (OD_{570}(\text{sample})/(OD_{570}(\text{control})) \times 100 \qquad (2)$$

All experiments were performed in triplicate, and repeated eight times for each concentration, and the data has been presented as mean

± S.D.

### 2.7. Flow cytometry analysis for the alterations in the cell cycle and apoptosis

Apoptosis was induced by treating the MCF-7 cells with $IC_{50}$ concentration of complex (**Rh3**), (26.29 µg/mL, 32.11 µM), for 24 h at 37 °C in 5% $CO_2$. Evaluation of apoptosis induction was performed in accordance with the Annexin V-FITC kit (eBioscience, USA Affymetrix). For this purpose, cells were collected by being transferred with the complete medium to 1.5 mL reaction tubes and were centrifuged at 1500 rpm for 5 min at 4 °C. These cells were then washed with 1 mL PBS and resuspended in 1 X binding buffer (Annexin V-FITC kit) by mixing 2 µL of Annexin-V and 2 µL of propidium iodide (PI) in the binding buffer according to the Annexin V-FITC kit. The cells were incubated for 15 min at room temperature, in dark. After centrifugation at 1500 rpm for 5 min at 4 °C, the staining buffer was aspirated and cells were resuspended in 100 µL PBS and were analyzed by the flow cytometry analysis immediately.

### 2.8. Cell-cycle analysis

For cell cycle analysis, the MCF-7 cells ($1 \times 10^6$) was cultured in two separate flasks, the treatment and the control. The cells of the treatment flask were incubated at a concentration of $IC_{50}$ of the **Rh3** complex, [Rh (ppy)$_2$(qbtz)]PF$_6$, (22.50 µg / mL) for 48 h, and were then separated from the flask with trypsin and washed with 2 mL sterile phosphate buffered saline (PBS). The resulting cellular deposition was collected in a falcon with centrifuge for 5 min at 1500 rpm. Lastly, 250 µL from a solution containing the color of PI and Triton-X100 detergent was added to the resulting cell precipitate. The cells were then incubated for 1 h in the dark at room temperature and analyzed by flow cytometry using the FlowJo software.

### 2.9. Analysis of apoptosis-related gene expression (miR-15, miR-16, miR-21, miR29, bcl-2, and p-53)

MCF-7 cells were treated with $IC_{50}$ concentration of complex (**Rh3**), 22.50 µg/mL, for 48 h. RNA extraction and cDNA synthesis were performed according to CinnaGen (Iran) and Revert AidTM First Strand cDNA Synthesis Kits (Fermentas) protocols, respectively. Briefly, the cells were lysed by RNX solution (Trizol reagent) (200 µL of chloroform was added to 1 mL of RNX solution) and were centrifuged at 12000 rpm, leading to the formation of three phases. The RNA molecule appeared in the upper phase and the protein and DNA were in the middle and lower phases, respectively. The highly transparent phase was transferred to a new vial and isopropanol, equal to the supernatant phase volume, was added and then centrifuged for 15 min at 12000 rpm. The supernatant was discarded and resulting pellet was dissolved in DEPC water. After confirming the quality and quantity of RNA, the cDNA synthesis was carried out according to the protocol of the Revert AidTM First Strand cDNA Synthesis Kit (Fermentas, Germany). In summary, 1–2 µg of the RNA, 1 µL of DNAase and 1 µL of 10X buffer were mixed and incubated at 37 °C for 30 min. 1 µL of EDTA was then added and incubated at 65 °C for 10 min to inactivate the DNAase enzyme activity. Subsequently, 4 µL of 5X buffer, 0.5 µL of RNasin (40 Unit/µL), 2 µL of dNTP mixture (10 mM), 2 µL of dT oligo, 1.5 µL of MgCl$_2$, and 1 µL of Reverse Transcriptase enzyme were added. The reaction mixture was placed in thermocycler for 60 min at 42 °C. The resulting samples were positioned in thermocycler for 10 min at 70 °C to deactivate RT enzyme. The reaction product was kept at − 20 °C. SYBER Green method was used to determine the expression of miR-15a, miR-16–1, miR-21, miR-29b, bcl-2, and p-53 genes in MCF-7 cells treated with **Rh3** complex after 48. The β-actin gene was used as internal control. The final volume of each reaction was considered 25 µL as follows; 12.5 µL of Mater mix (Bioneer, Korea), (0.1-1µg) 1 µL of synthesized cDNA of β-actin, miR-15, miR-16–1, miR-21, miR-29b, bcl-2, and p53 genes, (10 mM) 1 µL of forward and reverse primers for each gene (Takapuzist company), 9.5 µL of DEPC water. The sequence of primers is presented in Table S2. The PCR reaction for each gene was performed separately in triplicates. The Real Time PCR reaction was performed with the Bioneer exicycler 96 according to the following protocol; The temperature program was optimized as follows; pre-denaturation at 95 °C for 10 min; 40 cycles of denaturation at 95 °C for 20 s, annealing at 57 °C for 40 s and extension at 72 °C for 40 s. After the reaction, data was extracted from the device as Ct and gene expression was measured using ΔΔCt method by Rest software. The gene expression was then plotted using the SPSS version 19 and Graph pad prism software.

### 2.10. Confocal luminescence imaging of live cells

The MCF-7 cells were seeded at a density of $2 \times 10^6$ cells per mL onto 6-well glass-bottom plates and allowed to adhere for 24 h prior to imaging. After 1 day, the cells in four well were separately treated with 16 µg/mL of **qbtz** for 5 h and 16 and 32 µg/mL of (**Rh3**) for 2 and 5 h respectively. Afterwards, the cells were washed three times with PBS and fixed with 4% paraformaldehyde solution for 10 min at room temperature and then subjected to the luminescence imaging measurement. Using Leica TCS SPE confocal laser scanning microscope (Zeiss), the fluorescent intensity of the compound was determined (objective lens X60).

### 2.11. Statistical methods

Statistical analysis was performed by analysis of variance (One- and Two-Way ANOVA) or $t$ test using the SPSS version 23 and the Prism version 5 software.

## 3. Results and discussion

### 3.1. Complex design, synthesis and characterization

The new ligand **pzbtz**, and the two previously reported **pybtz** and **qbtz** ligands, were prepared in a one pot synthesis according to a simple and benign synthetic method developed in our laboratory (Scheme 2) [41].

The dichloro-bridged dinuclear cyclometalated rhodium(III) precursor, [Rh(ppy)$_2$Cl]$_2$ (ppy: 2-phenylpyridine), was synthesized using a previously reported procedure [46]. Preparation of the cationic [Rh (C^N)$_2$(N^N)]PF$_6$ complexes, **Rh1-Rh3**, were carried out through concomitant bridge-splitting reaction of [Rh(ppy)$_2$Cl]$_2$ and complexation with the **pybtz**, **pzbtz** and **qbtz** ligands in refluxing CH$_2$Cl$_2$/EtOH solution.

The as synthesized **pzbtz** ligand and Rh(III) complexes (**Rh1-Rh3**) were characterized using elemental analysis, FT-IR, UV–vis, and $^1$H NMR spectroscopy (see ESI, Fig. S1–S13). The $^1$H NMR spectrum of the **pzbtz** ligand recorded in CDCl$_3$ showed the seven aromatic protons appearing as five doublets (H$_{g,e,f,d,a}$) and two triplets (H$_{b,c}$), Fig. S7. The $^1$H NMR spectra of the **Rh1** and **Rh2** complexes were measured in DMSO-$d_6$ and **Rh3** spectrum in CDCl$_3$. The $^1$H NMR spectra of **Rh1-Rh3** complexes, display three well-resolved broad doublets in the aromatic region between 6.14 and 6.76 ppm, corresponding to the H$^1$, H$^2$, and H$^3$ protons of phenylpyridine (Scheme 1). These protons appear at 6.17, 6.29, and 6.75 for **Rh1**, 6.14, 6.24, and 6.76 for **Rh2**, and 6.31, 6.38, and 6.64 for **Rh3** respectively. The signals due to the protons of the ancillary benzothiazole ligands are partially overlapping with the signals of the cyclometalated 2-phenylpyridine ligands. However, H$^4$ appears as a well resolved broad doublet at 8.71 for **Rh1** and 8.97 for **Rh2**. Moreover, H$^4$ and H$^5$ appear as two broad doublets at 8.59 and 8.79 ppm for **Rh3** [47]. Due to the asymmetric structure of the **Rh1-Rh3** complexes, the interpretation of proton NMR data for these complexes in the range of 6.93–8.86 ppm is very complicated and a clear assignment of
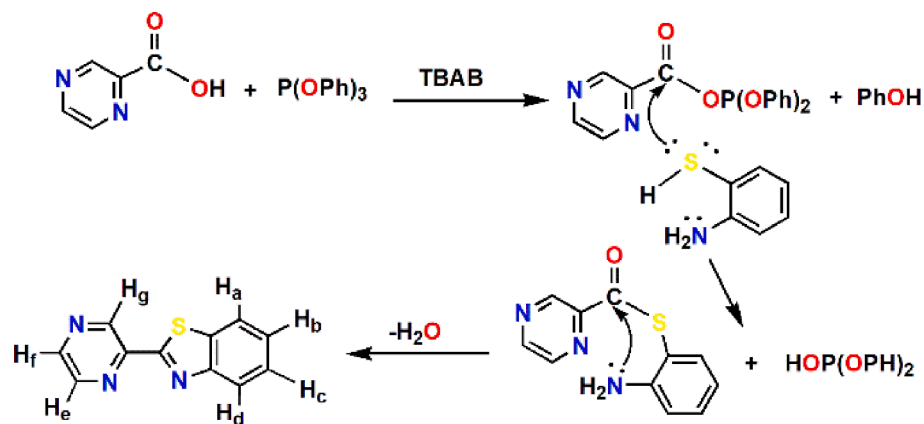
**Scheme 2.** Proposed reaction mechanism for **pzbtz** ligand synthesis [35].

interproton distances generated by the NMR experiment is not readily accomplished. The existence of a common pattern in the $^1$H NMR spectra of **Rh1**, **Rh2**, and **Rh3** suggest similar structures for all three [Rh(CˆN)$_2$(NˆN)]PF$_6$ complexes. The $^1$H NMR spectra and elemental analysis data of these complexes conform to the assigned distorted octahedral structures of **Rh1** and **Rh3** obtained by a single-crystal X-ray structure determination.

### 3.2. Crystal and molecular structures of Rh1 and Rh3

Single crystals of **Rh1** and **Rh3** were obtained from dichloromethane-methanol and dichloromethane-ethanol respectively by slow evaporation of the solvents. The diffraction experiment was performed on a Bruker Kappa ApexII diffractometer (for more details see ESI). The X-ray crystal structures of the two complexes are presented in Fig. 1 and Fig. 2. The solvate complex [Rh(ppy)$_2$(pybtz)]PF$_6$.MeOH (**Rh1**.MeOH) crystalizes in the monoclinic space group $P2_1/n$ (no. 14) and [Rh(ppy)$_2$(qbtz)]PF$_6$ (**Rh3**) crystalizes in the monoclinic space group $Cc$ (no. 9). The coordination geometry around Rh atoms is comprised of the C and N atoms of the two phenylpyridine ligands and two N atoms of the benzothiazole derivative. Selected bond length and angels are listed in Table 1. In the two rhodium complexes the trans
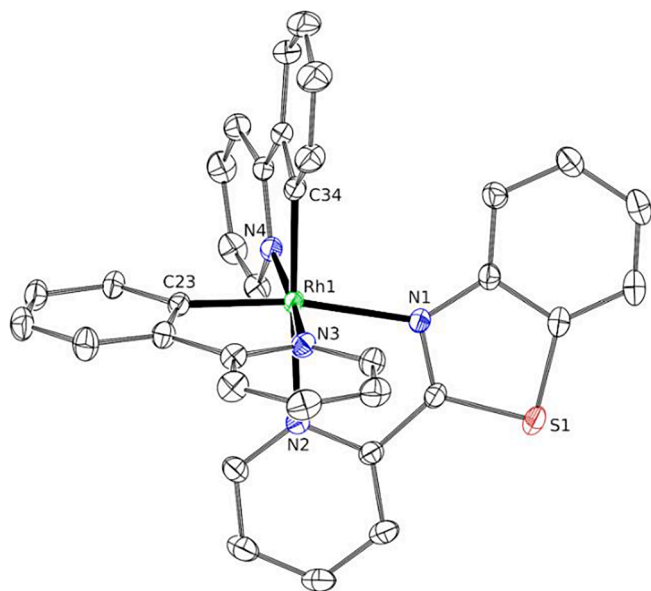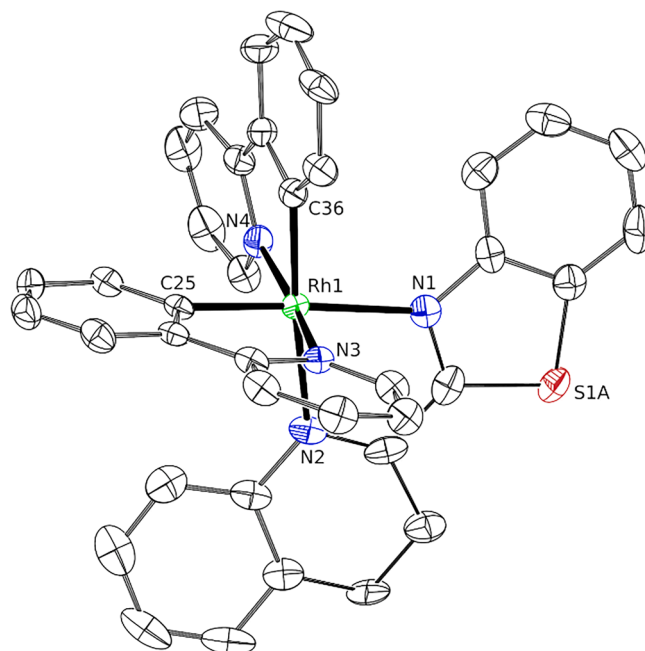


**Fig. 2.** X-ray crystal structure of complex **Rh3** with the displacement ellipsoids drawn at the 50% probability level. The minor disorder component of the **qbtz** ligand, hydrogen atoms and PF$_6^-$ counter-ion have been omitted for clarity.

angels range from 169.85(4)° to 176.39(18)° while the cis angles are between 75.23(14)° and 103.18(14)°, and the order of bond distances are Rh-C < Rh-Nppy < Rh-Nbtz indicating distorted octahedral geometry around the central Rh atom.

The ppy cyclometallating ligand, of which the coordinating C23 atom is trans to the benzothiazole unit, is nearly planar for **Rh1** with angle between the two ring planes of 1.6°, but shows slight deviation from planarity for **Rh3** (5.6°). The angles between the ring planes of the other ppy ligand (coordinating C34 atom trans to the pyridine ring of the ancillary ligand) are 9.7 and 10.4° for **Rh1** and **Rh3** respectively, indicating noticeable deviation from planarity in this ligand. However, the **pybtz** ancillary ligand in **Rh1**.MeOH and the **qbtz** in **Rh3** are distorted from planarity (with almost equal angles between the ring planes = 5.5 and 5.8° respectively).

### 3.3. Electronic absorption spectroscopy

The electronic absorption spectra of the **pybtz**, **pzbtz** and **qbtz** ligands (Fig. S11-S13) and their cyclometalated Rh(III) complexes were



**Fig. 1.** X-ray crystal structure of complex **Rh1** with the displacement ellipsoids drawn at the 50% probability level. The solvent molecules, hydrogen atoms and PF$_6^-$ counter-ion have been omitted for clarity.

**Table 1**
Selected bond lengths (Å) and bond angles () of **Rh1** and **Rh3** complexes.

| *Bond lengths* (**Rh1**) | | | |
|---|---|---|---|
| Rh–C23 | 1.9889(10) | Rh–N3 | 2.0480(9) |
| Rh–C34 | 1.9978(10) | Rh–N2 | 2.1689(9) |
| Rh–N4 | 2.0395(9) | Rh–N1 | 2.1942(9) |
| *Bond angles* (**Rh1**) | | | |
| C23–Rh1–C34 | 87.92(4) | N4–Rh1–N2 | 96.57(3) |
| C23–Rh1–N4 | 92.49 (4) | N3–Rh1–N2 | 88.74(4) |
| C34–Rh1–N4 | 81.35(4) | C23–Rh1–N1 | 169.85(4) |
| C23–Rh1–N3 | 81.29(4) | C34–Rh1–N1 | 100.86(4) |
| C34–Rh1–N3 | 93.64(4) | N4–Rh1–N1 | 93.85(3) |
| N4–Rh1–N3 | 172.19(3) | N3–Rh1–N1 | 92.97(3) |
| C23–Rh1–N2 | 95. 15(4) | N2–Rh1–N1 | 76.27(3) |
| C34–Rh1–N2 | 176. 38(4) | | |
| *Bond lengths* (**Rh3**) | | | |
| Rh–C36 | 1.989(4) | Rh–N3 | 2.051(3) |
| Rh–C25 | 2.006(4) | Rh–N1 | 2.216(4) |
| Rh–N4 | 2.042(3) | Rh–N2 | 2.226(3) |
| *Bond angles* (**Rh3**) | | | |
| C36–Rh1–C25 | 81.26(15) | N4–Rh1–N1 | 92.40(12) |
| C36–Rh1–N4 | 81.49(15) | N3–Rh1–N1 | 95.25 (12) |
| C25–Rh1–N4 | 91.04(15) | C36–Rh1–N2 | 175.56(15) |
| C36–Rh1–N3 | 92.02(14) | C25–Rh1–N2 | 103.18(14) |
| C25–Rh1–N3 | 81.43(15) | N4–Rh1–N2 | 98.42(12) |
| N4–Rh1–N3 | 170.76(13) | N3–Rh1–N2 | 88.57(11) |
| C36–Rh1–N1 | 100.33(14) | N1–Rh1–N2 | 75.23(14) |
| C25–Rh1–N1 | 176.39(18) | | |

recorded in DMSO:$H_2O$ (1:1 v/v) at room temperature (Fig. 3). Peak positions and molar absorption coefficients (ε) from these spectra are listed in Table 2. Comparing the optical features of **Rh1**-**Rh3** complexes and benzothiazole ligands (Table 2), the absorption spectra of these complexes are identified by superposition of the shifted intraligand spin-allowed (π-π*) transitions of the cyclometalated ppy and ancillary benzothiazole ligands. For the **Rh1**-**Rh3** complexes, the high intensity bands with $19550 < \varepsilon < 95380$ M$^{-1}$ cm$^{-1}$, appearing below 360 nm, are assigned to spin-allowed ligand-centered $^1$LC ($^1$π-π*) transitions, localized on the coordinated ppy and benzothiazole. While, the low intensity bands showing up at lower energy, in the range $360 < \lambda < 500$ nm, with $\varepsilon < 12500$ M$^{-1}$ cm$^{-1}$ do not conform to $^1$π-π* allowed transitions and are far more complicated.

Considering the strong filed ppy ligands, *d-d* transitions are not likely to appear in the lower energy region. Moreover, it is well documented that in comparison to iridium(III), oxidation of the rhodium(III) cyclometalated complexes (see Electrochemical properties, *vide infra*) is difficult [35,48,49] and pure MLCT cannot occur readily by low energy excitation. So, the lower energy bands can be due to the charge transfer transitions that originate from a HOMO which may result from a strong admixture of a σ-bonding ligand orbital and a d$_\sigma$ (e$_g$) metal orbital. This transition can reasonably be assigned to $^1$SBLCT (σ-bond-to-ligand charge transfer) [35–37,48,49].

*3.4. Luminescence properties*

Both **Rh1** and **Rh3** complexes were found to luminesce in DMSO: $H_2O$ (1:1 v/v) upon irradiation at room temperature (Fig. 4). The emission data of these complexes and their ancillary benzothiazole ligands are summarized in Table 2. The room temperature excitation of the **Rh1** and **Rh3** complexes in DMSO: $H_2O$ (1:1 v/v) at 400 and 410 nm respectively, leads to strong emission with red shift relative to the corresponding benzothiazole ligands (Fig. S14 and S16). It should be noted that **Rh3**, bearing the ligand of largest π-conjugation, also has the strongest absorbance and emission intensity as indicated by its higher quantum efficiency, Φ = 0.03 (Table 2).

Although all three complexes have the same "(ppy)$_2$Rh'' fragment, the emission characteristic of **Rh2** complex, containing pyrazolyl-benzothiazol ligand, is different from **Rh1** and **Rh3** complexes, showing no emission in the visible region. This is presumably due to the
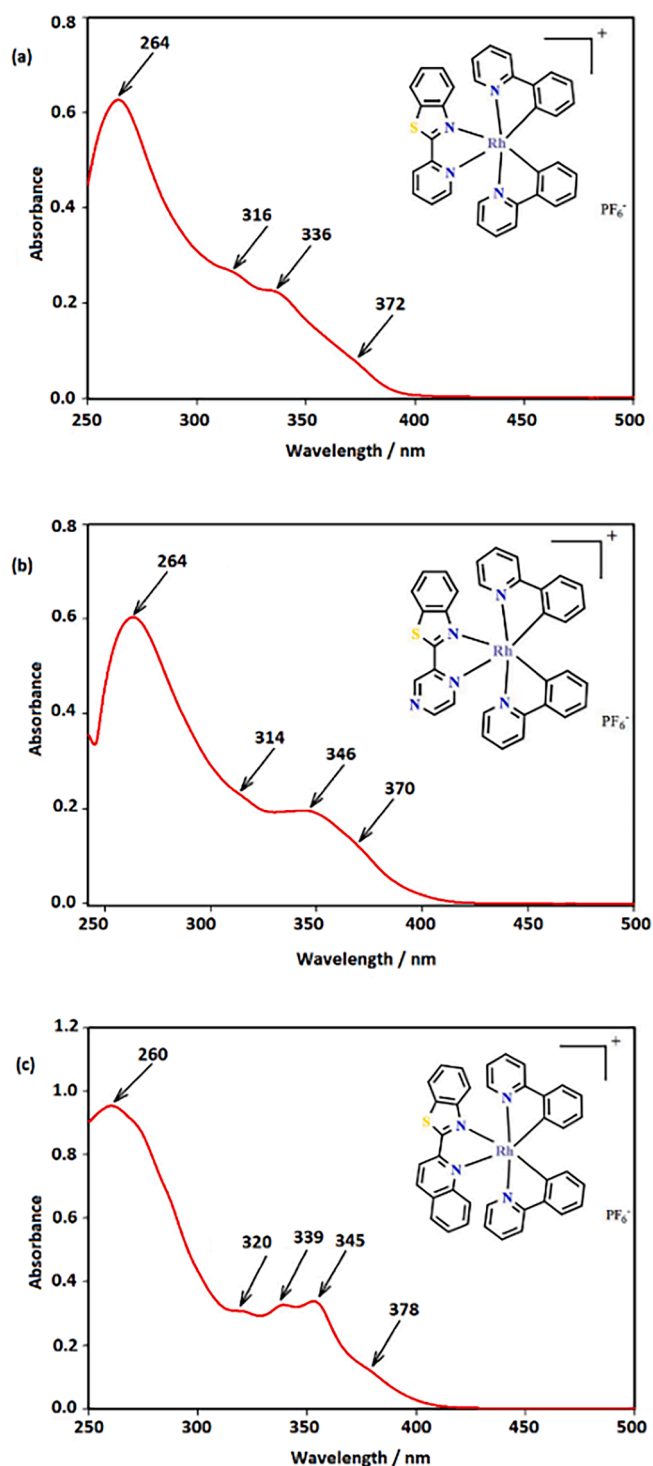


**Fig. 3.** Ground-state absorption spectra for the (a) **Rh1**, (b) **Rh2**, and (c) **Rh3** complexes in DMSO:$H_2O$ (1:1 v/v) at room temperature.

intersystem crossing to a nonemissive excited state, having a major contribution from the additional nitrogen atom of the pyrazolyl moiety in **Rh2** [50]. It is interesting to note that the emission intensity of **pzbtz** (Fig. S15), the free ancillary ligand of **Rh2**, is about one fourth of the free ancillary ligands of **Rh1** and **Rh3** (**pybtz** and **qbtz**). These observations indicate that the aforementioned emissive state is apparently centred on the ancillary benzothiazole ligand and are in accord with analogous iridium complexes that are presented elegantly by H. J. Bolink *et al.* [39].

**Table 2**

UV–Vis absorption and emission data in DMSO: $H_2O$ (1:1 v/v) at 298 K (for more details see ESI).

| Compounds | Absorption (RT) | | Emission (RT) | | |
|---|---|---|---|---|---|
| | $\lambda_{max}$ nm | $\varepsilon$ $M^{-1}cm^{-1}$ | $\lambda_{ex}$ nm | $\lambda_{max}$ nm | $\Phi$ |
| **pybtz** | 270 | 51,030 | 340 | 396 | – |
| | 312 | 20,730 | | | |
| | 327 | 14,050 | | | |
| **pzbtz** | 274 | 14,850 | 350 | 436 | – |
| | 322 | 16,370 | | | |
| **qbtz** | 276 | 19,810 | 360 | 416 | – |
| | 286 | 20,230 | | | |
| | 324 | 17,630 | | | |
| | 338 | 20,900 | | | |
| | 352 | 18,870 | | | |
| **Rh1** | 264 | 62,760 | 400 | 524 | 0.023 |
| | 316 | 26,710 | | 551 | |
| | 336 | 22,510 | | | |
| | 372 | 8080 | | | |
| **Rh2** | 264 | 60,340 | – | – | – |
| | 314 | 22,920 | | | |
| | 346 | 19,550 | | | |
| | 370 | 11,950 | | | |
| **Rh3** | 260 | 95,380 | 410 | 543 | 0.03 |
| | 320 | 30,720 | | 584 | |
| | 339 | 32,610 | | | |
| | 354 | 33,750 | | | |
| | 378 | 12,480 | | | |



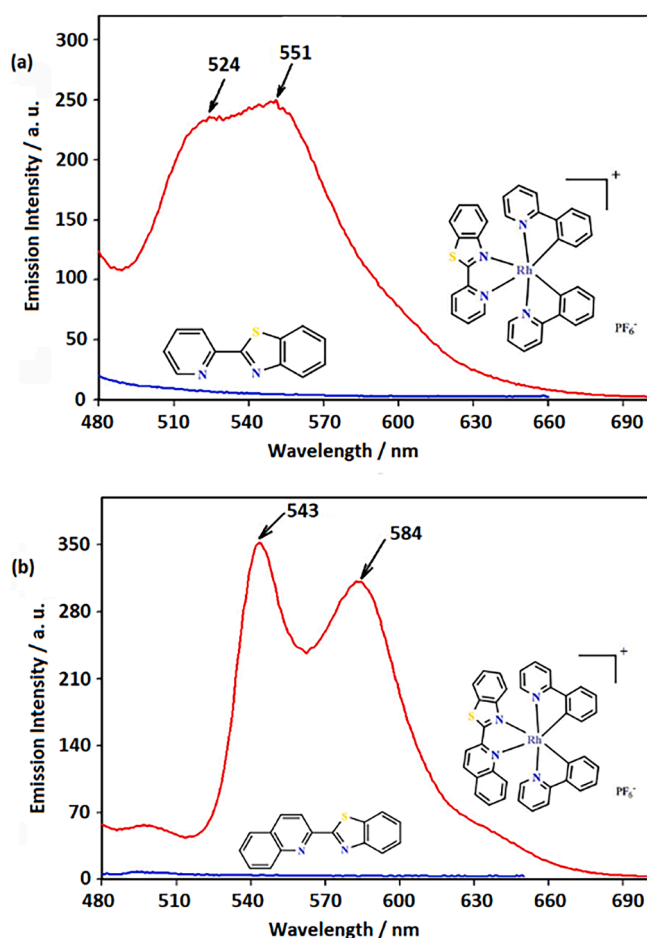**Fig. 4.** Emission spectra of (a) **Rh1** ($\lambda_{ex}$ = 400 nm) and (b) **Rh3** ($\lambda_{ex}$ = 410 nm) in $H_2O$:DMSO (1:1 v/v) at room temperature (red) and their ancillary ligands (blue) in 480–700 nm region. (For interpretation of the references to color in this figure legend, the reader is referred to the web version of this article.)

### 3.5. Electrochemical properties

Electrochemical studies of the ligands **pybtz**, **pzbtz**, and **qbtz** and their corresponding **Rh1-Rh3** complexes in acetonitrile solution were carried out by cyclic voltammetry at room temperature. The cyclic voltammograms are depicted in Fig. S17-S22 and the electrochemical data are listed in Table 3. As illustrated in Fig. S17-S19 the **pybtz**, **pzbtz** and **qbtz** ligands display two reduction processes at ca. − 1.39 to − 2.49 V versus SCE, which are related to the reduction of benzothiazole and pyridyl units of the ligands. The first reduction potentials observed in the cyclic voltammograms of these ligands (**pzbtz**: −1.51 V < **qbtz**: −1.61 V < **pybtz**: −1.91 V) are consistent with their structural differences. Evidently, the presence of the electron withdrawing pyrazinyl and quinolinyl units in **pzbtz** and **qbtz** ligands have led to the reduction of benzothiazole moiety at less negative potentials in comparison with **pybtz**. These features, slightly shifted towards negative potentials, are also observed in the cyclic voltammograms of **Rh1**, **Rh2**, and **Rh3** complexes. All three complexes show two reversible couples in the potential ranges of − 0.93 to − 1.19 V and − 1.62 to − 1.83 V (Fig. 5), which may be assigned to the reduction of $Rh^{III/II}$ and $Rh^{II/I}$, respectively. The peaks with the low current intensity between − 0.4 - −0.8 V correspond to the reduction of the byproducts resulting from the irreversible oxidation processes at the potentials around + 1.5 V. The π system of benzene ring of the ligands **pybtz**, **pzbtz**, and **qbtz**, is the expected site of oxidation at these potentials, generating a cation radical as the byproduct. The existence of similar reduction waves is documented in several papers published by our research group and other researchers on the electrochemistry of closely related ligands and their metal complexes, Fig. S22-2 (see ESI for details) [51].

In general, the tendency of the Rh(III) centre with respect to reduction is: **Rh1** < **Rh3** < **Rh2**, demonstrating the electron-donating character of the coordinated benzothiazole ligands as follows: **pzbtz** < **qbtz** < **pybtz**. In addition, this behavior conforms to the structural data obtained from X-ray diffraction for the two complexes **Rh1** and **Rh3** (Table 1). The bond lengths of Rh-N1 (2.1942(9) Å) and Rh-N2 (2.1689 (9) Å) in **Rh1** are shorter than Rh-N1 (2.216(4) Å) and Rh-N2 (2.226(3) Å) in **Rh3**. The observed electrochemical data are consistent with those reported for related Rh(III) complexes [52,53]. The quasi-reversible or irreversible waves appearing at more negative potentials are ascribed to the reduction of the coordinated ancillary benzothiazole and the cyclometalating ppy ligands [54].

Moreover, **Rh1-Rh3** complexes exhibit an irreversible oxidation wave at ca. + 1.56, +1.55, and + 1.53 V, respectively, assigned to an admixture of metal ($Rh^{III/IV}$) and ligand (benzene ring) centred oxidation processes [36,49,55,56]. Irreversible metal-centered oxidation waves have been observed in cyclometalated Ir(III) and Rh(III) complexes, especially in those that have HOMOs associated with metal–ligand character [57–59]. The appearance of a weak shoulder at + 1.43 V in **Rh3** is attributable to the oxidation of the second benzene ring of quinoline (Fig. 5 and Fig. S22). As reported in similar rhodium complexes [36], the irreversible oxidation wave observed in the **Rh1-Rh3** complexes suggests that the electron removed in this process originates from a Lσ-dσ bonding orbital, and irreversibility in this case is apparently due to subsequent cleavage of the Rh-C bond. This formulation suggests that the absorption bands appearing at about 370–380 nm might be due to $^1$SBLCT transitions (*vide supra*) in which an electron is promoted from the Lσ-dσ bonding orbital (HOMO) to a π* orbital of a ligand (LUMO).

### 3.6. Theoretical calculations

Lipophilicity is an important parameter for biochemical, pharmacological and environmental processes in quantitative structure–activity relationship (QSAR) studies [60]. The cytotoxicity of the compounds is dependent on their lipophilicity, and is increased by raising their lipophilicity. The logarithm of the partition coefficient of a drug between 1-

**Table 3**

Electrochemical data of complexes **Rh1**-**Rh3** in $CH_3CN$ and referenced to $Fc/Fc^+$.

| Compounds | $E_{ox}$ | $E_{red1}(E_{ox1})$ | $E_{red2}(E_{ox2})$ | $E_{red3}(E_{ox3})$ | $E_{red4}(E_{ox4})$ |
|---|---|---|---|---|---|
| $[Rh(ppy)_2(bpy)]^+$ [a] | +1.42 | −1.49 | – | – | – |
| $[Rh(ppy)_2(pybtz)]^+$ (**Rh1**) | +1.56 | −1.19(−1.12) | −1.83(−1.71) | −2.08(−1.98) | −2.18(−2.09) |
| $[Rh(ppy)_2(pzbtz)]^+$ (**Rh2**) | +1.55 | −0.93(−0.86) | −1.62(−1.50) | −1.99(−1.90) | −2.16(−2.05) |
| $[Rh(ppy)_2(qbtz)]^+$ (**Rh3**) | +1.5, +1.43 | −1.01(−0.94) | −1.64(−1.56) | −1.99(−1.88) | – |

([a]) From Ref. [36]
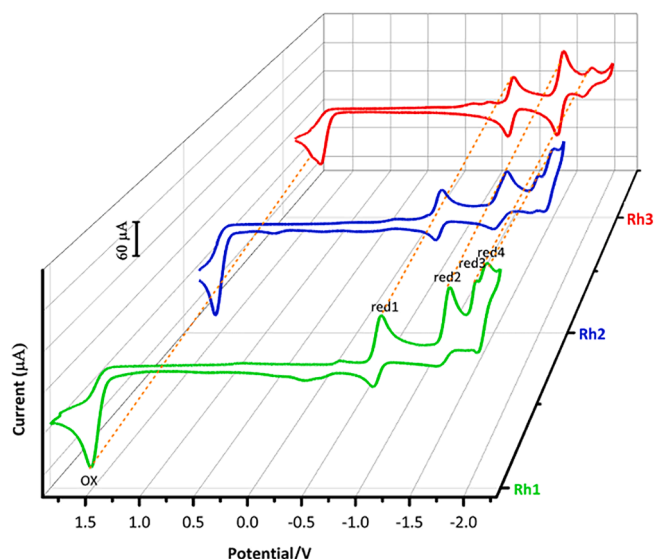


**Fig. 5.** Cyclic voltammograms of complexes (a) **Rh1**, (b) **Rh2**, and (c) **Rh3** in $CH_3CN$ ($10^{-3}$ M).

octanol and water (log $P_{o/w}$) is a commonly accepted physicochemical parameter for its important biological effects, and is extensively used in medicinal chemistry. Thus, estimation of log $P_{o/w}$ is necessary for the design of new drugs. Since log $P_{o/w}$ has become a significant hydrophobic parameter, numerous experimental and theoretical methods have been developed to measure or calculate log $P_{o/w}$ for the molecules that may have the potential of being used as drugs. In order to estimate the lipophilicity of **qbtz** ligand and **Rh1**-**Rh3** complexes, the geometries of these compounds were optimized in water and 1-octanol as solvents using DFT-M06L/6–31 + G(d) and DFT-M06L/6–31 + G(d)/LANL2DZ level of theory for the ligand and complexes, respectively. For predicting their toxicities, the common log $P_{o/w}$ of the **qbtz** ligand and the rhodium complexes was then calculated by computing the $\Delta G$ of solvation in water ($\Delta G_{solv(water)}$) and 1-octanol ($\Delta G_{solv(1-octanol)}$) solutions at the same functional and basis set, using equation (1). In accordance with the calculated log $P_{o/w}$ values that associate with log $(1/IC_{50})$ given in Table 4, the order of log $P_{o/w}$ for the **Rh1**-**Rh3** complexes is **Rh3** > **Rh1** > **Rh2**. The log $P_{o/w}$ values reveal that **Rh3**, with the log $P_{o/w}$ value of 8.28, is expected to show the highest toxicity relative to **Rh1** and **Rh2** complexes as well as its ancillary ligand, presumably due to its higher

**Table 4**

Calculated solvation free energy change in going from the gas phase to water phase ($\Delta G_{solv(water)}$ / kcal mol$^{-1}$) and 1-octanol phase ($\Delta G_{solv(1-octanol)}$ / kcal mol$^{-1}$), examined at M06L/6–31 + G(d)/ LANL2DZ level of theory under standard state conditions, and the corresponding log $P_{O/W}$ values.

| Compounds | $\Delta G_{solv(water)}$(kcal mol$^{-1}$) | $\Delta G_{solv(1-octanol)}$(kcal mol$^{-1}$) | $\Delta G_{o/w}$(kcal mol$^{-1}$) | Log $P_{o/w}$ |
|---|---|---|---|---|
| **qbtz** | −10.03 | −12.42 | −2.40 | 1.75 |
| **Rh1** | −33.93 | −44.24 | −10.31 | 7.56 |
| **Rh2** | −37.99 | −45.69 | −7.70 | 5.64 |
| **Rh3** | −33.18 | −44.47 | −11.30 | 8.28 |

hydrophobicity originating from the additional benzene ring in its ancillary ligand, **qbtz**. Based on these observations, **Rh3** with a higher lipophilicity effect, relative to **Rh1** and **Rh2** complexes, was selected for biological studies. This complex was then used for the determination of $IC_{50}$ (i.e., the concentration required to inhibit 50% of cells from growing) on a panel of human cancer cell line, breast adenocarcinoma MCF-7 cells, and for comparison with its benzothiazole ancillary ligand, **qbtz**. The cationic character of this complex contributes to more efficient cell membrane permeability (*vide infra*).

### 3.7. Cell viability analysis

The octahedral metal complexes, as compared to the organic compounds, show unique features that render them applicable as inhibitors of specific biomolecular targets. In contrast to the organic molecules that are mainly limited to linear, trigonal planar, and tetrahedral geometries, these complexes provide a favorable geometry for the precise arrangement of co-ligands. Moreover, the steric and electronic properties of metal complexes can be finely tuned by facile synthetic methods. These features may facilitate the octahedral metal complexes to approach the regions of the chemical space in protein binding pockets that are inaccessible to purely organic molecules. In this context, the influence of the *in vitro* antiproliferation of **qbtz** ligand, as an organic molecule, and **Rh3** octahedral complex on the malignant (MCF-7) and non-malignant (MRC-5) cell lines were evaluated by MTT assay [61]. The MTT results of MCF-7 and MRC-5 cells were compared with each other as well as with the control. In order to discriminate between the effects of **qbtz** ligand and **Rh3** cationic complex on both MCF-7 cell line and MRC-5 cells, the cells were treated in the presence of **qbtz** and **Rh3** with various concentrations of 2, 4, 8, 16, and 32 μg/mL and incubation periods of 24, 48 and 72 h. The results of MTT analysis and induction of cytotoxicity are exhibited in Fig. 6 (a, b, c, d). MTT assay was performed in octuplicate, and the results are presented as mean ± S.D. of three independent experiments.

The cytotoxicity of both **qbtz** and **Rh3** are statistically significant compared to the control ($p < 0.0001$) in both MCF-7 and MRC-5 cell lines. These results clearly demonstrate that the cytotoxic effect of **qbtz** ligand and **Rh3** cyclometalated complex on MCF-7 breast cancer cells is dose and exposure time dependent ($p < 0.0001$). Although, comparing to the control group, there is no significant cytotoxic effect of **Rh3** on non-malignant MRC-5 cells, the viability of MCF-7 cells decreases significantly after treatment with **Rh3** complex (Fig. 6). As evident from Fig. S23, the cytotoxic effect of **qbtz** and **Rh3** on MRC-5 cells and **qbtz** on MCF-7 cells at their highest concentration (32 ppm) increased by approximately 1.5-fold as compared to the lowest concentration (2 ppm) for all incubation times. However, the increase in the cytotoxic effect of **Rh3** on MCF-7 breast cancer cells, in going from 2 to 32 ppm, is about 3-fold after 24 and 48 h culture and about 5-fold after 72 h. These results are in agreement with the dose determinant characteristics of analogous cyclometalated Rh complex reported by Zhong *et al.* [12]. In general, the cytotoxicity of the **Rh3** complex is higher than its free ancillary ligand **qbtz** in both cancer and healthy cell lines, MCF-7, and MRC-5 cells, and significantly higher at 32 μg/mL for all incubation times in MCF-7 cell line (Fig. S24).

The $IC_{50}$ values of **qbtz** and **Rh3** after 24, 48 and 72 h of exposure time for the MCF–7 and MRC-5 cells are listed in Table 5. As evident
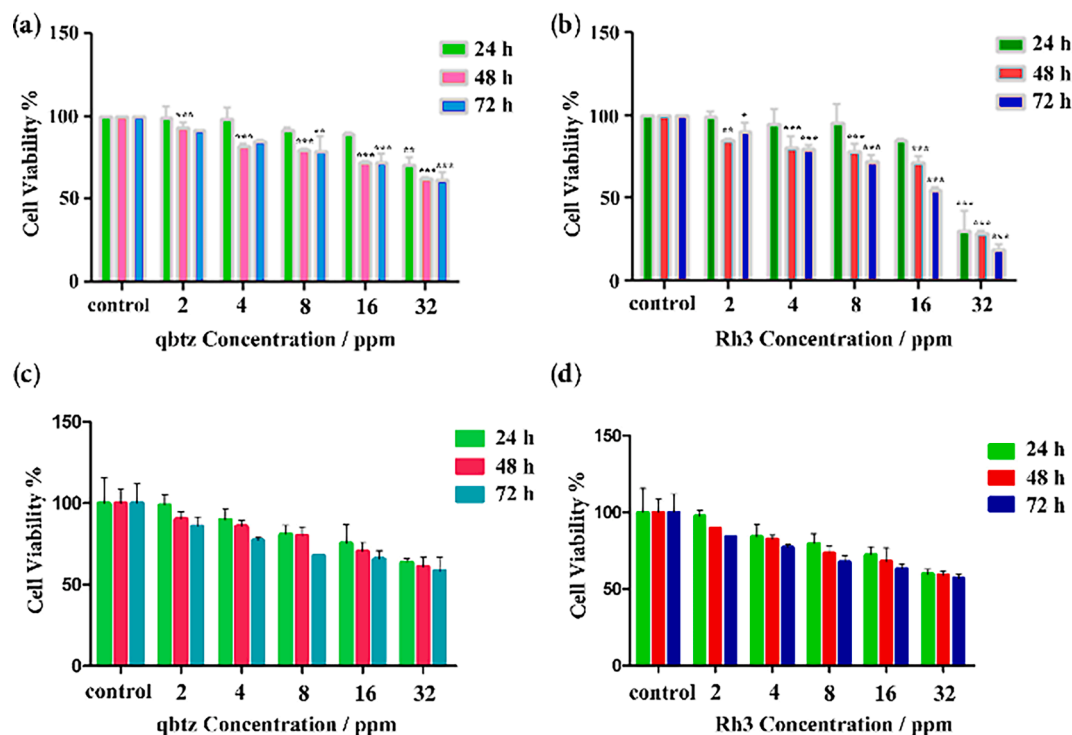
**Fig. 6.** Effect of qbtz ligand and **Rh3** complex on cell viability of MCF-7 and MRC-5 cells. The results of the MTT assay in MCF-7 cell line treated with (a) **qbtz** ligand and (b) **Rh3** complex and in MRC-5 cells treated with (c) **qbtz** ligand and (d) **Rh3** complex after 24, 48 and 72 h (results are reported as viability in comparison with control samples) [$p \leq 0.001$***, $p \leq 0.01$**, $p \leq 0.05$*] (n = 3) (based on Two-way ANOVA statistical method).

**Table 5**

IC$_{50}$ values of **qbtz** and Rh3 from all incubation times for MCF-7 and MRC-5 cell lines.

| MCF-7 cell line | | | | |
|---|---|---|---|---|
| Compound | | qbtz | Rh3 | Cisplatin[a] |
| IC$_{50}$ (24 h) | μM | 212.86 ± 5.14 | 32.11 ± 2.26 | - |
| | μg/mL | 55.84 ± 1.35 | 26.29 ± 1.85 | |
| IC$_{50}$ (48 h) | μM | 158.19 ± 5.71 | 27.48 ± 2.02 | – |
| | μg/mL | 41.05 ± 1.50 | 22.50 ± 1.66 | |
| IC$_{50}$ (72 h) | μM | 149.43 ± 3.65 | 22.47 ± 1.40 | 23.00 |
| | μg/mL | 39.20 ± 0.96 | 18.40 ± 1.15 | - |
| IC$_{50}$ (Mean) | μM | 172.91 ± 4.84 | 27.35 ± 1.89 | – |
| | μg/mL | 45.36 ± 1.27 | 22.39 ± 1.55 | - |
| MRC-5 cell line | | | | |
| Compound | | qbtz | Rh3 | |
| IC$_{50}$ (24 h) | μM | 157.66 ± 4.11 | 45.85 ± 1.13 | |
| | μg/mL | 41.36 ± 1.08 | 37.54 ± 0.93 | |
| IC$_{50}$ (48 h) | μM | 147.25 ± 2.82 | 44.12 ± 2.04 | |
| | μg/mL | 38.63 ± 0.74 | 36.12 ± 1.67 | |
| IC$_{50}$ (72 h) | μM | 132.80 ± 7.28 | 40.44 ± 1.49 | |
| | μg/mL | | 33.11 ± 1.22 | |
| | | 34.84 ± 1.91 | | |
| IC$_{50}$ (Mean) | μM | 145.92 ± 4.72 | 43.47 ± 1.55 | |
| | μg/mL | 38.28 ± 1.24 | 35.59 ± 1.27 | |

[a] Ref. [62].

from Table 5, the mean IC$_{50}$ values in various incubation times of the MCF-7 cell line for **Rh3** is reduced by approximately 6.5-fold relative to **qbtz** indicating that the cytotoxicity of the **Rh3**, as a kinetically inert octahedral metal complex, is more than the purely organic molecule **qbtz**. Similarly, the **Rh3** complex showed higher cytotoxicity on healthy MRC-5 cell line than **qbtz** ligand. It is interesting to note that, based on the mean IC$_{50}$ values, the organometallic complex **Rh3** shows a notable cytotoxicity against MCF-7 cancer cells, which is 1.6 times more than its toxicity on healthy MRC-5 cells (Fig. S25) and comparable to cisplatin [62]. Moreover, by increasing the incubation time from 24 to 72 h, the difference in the toxicity of this complex on MCF-7 cancer cells

compared to healthy MRC-5 cells increased and changed from 1.4 to 1.8-fold. It shows that the side effects of this compound on healthy cells are less as compared to its toxicity on cancer cells with increasing exposure time.

### 3.8. Induction of apoptosis in MCF-7 cells treated with [Rh(ppy)$_2$(qbtz)] PF$_6$, Rh3

The cell proliferative inhibition with induction of apoptosis is one of the important approaches in designing new chemotherapy drugs in the cancer treatment. It is noteworthy that in recent developments a number of kinetically inert rhodium(III) complexes have been used as protein inhibitors in regulating essential cellular processes, such as cell growth, proliferation, survival, and metabolism [13,63,64]. These results inspired us to study the mode of cell death by **Rh3** on the breast cancer cell line, MCF-7. So, to determine whether the mode of cell death induced by **Rh3** is apoptosis or necrosis, the effect of **Rh3** on MCF-7 was evaluated by flow cytometry technique using Annexin V/PI double staining. During the programed cell death or apoptosis, phosphatidylserine is transferred from the inner surface to the outer surface of the cell membrane. Apoptosis can then be detected using Annexin dye which, after binding to phosphatidylserine on the extracellular surface, is identified by flow cytometry. In the case of necrosis and late apoptosis, propidium iodide (PI) is attached to the fragmented DNA of the nuclei of the cells and is also detectable by a flow cytometer. The percentage of the cell populations in each of the distinct quadrants including Q1-Q4 portions were statistically determined. Q1 (Annexin V−/PI + ), Q2 (Annexin V+/PI + ), Q3 (Annexin V+/PI − ) and Q4 (Annexin V−/PI − ) represent necrotic cells, late apoptotic cells, early apoptotic cells, and viable cells respectively (Fig. 7).

The MCF-7 cancer cells were treated by the IC$_{50}$ concentration of **Rh3** (26.29 μg/mL) for 24 h. The untreated cells were considered as the control. As listed in Table S3, the rate of early and late apoptosis in the treated MCF-7 cells increased significantly ($p < 0.01$ and $p < 0.001$) by about 14 and 61-fold respectively, as compared to the control. The total
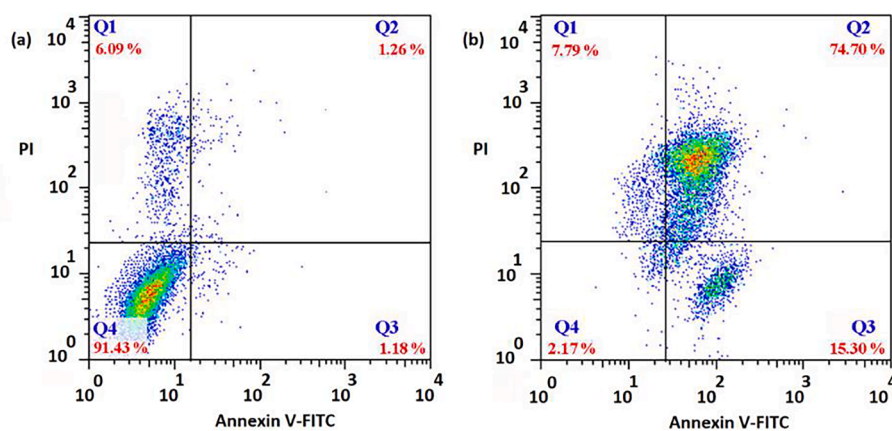
**Fig. 7.** Flow cytometry chart for evaluating apoptosis induced by **Rh3** in 24 h. (a) control cells (untreated cells) and (b) treated cells at 26.29 μg/mL (IC$_{50}$ value). Q1: necrotic cells with Annexin V/FITC − and PI + staining index, Q2: late apoptotic cells with Annexin V/FITC + and PI + index, Q3: early apoptotic cells with Annexin V/FITC + and PI − staining index and Q4: healthy cells with Annexin V/FITC − and PI − staining index.

percentage of cells located in Q2 and Q3 regions represent the percentage of total apoptosis and can be compared with cells located in the Q1 region (representing necrotized cells) (Table S4). The increase in the necrotic death of the treated cells with **Rh3** relative to non-treated control cultures was not that significant ($p > 0.05$) (Table S3). The results clearly show that **Rh3** significantly induces cell apoptosis with highest potency against MCF-7 cancer cells at 24 h of exposure and the observation is in agreement with the *in vitro* MTT results.

### 3.9. Cell-cycle arrest

The anticancer drugs are able to cause cell death through induction of programed cell death [65], or inhibition of the cell-cycle mechanism [66,67]. The cell-division cycle includes two brief periods: the interphase (I) consisting of the three main subdivisions: G1 (gap1); S (synthesis); G2 (gap2), in which the cell grows and duplicates its DNA, and the mitosis (M) phase, in which the cell divides into two separate cells. In the evaluation of the anticancer activity of **Rh3** through apoptosis, the effect of **Rh3** on the MCF-7 cell cycle distribution profile was further examined for verifying the suppression of cancer cell proliferation by cell cycle arrest and confirming the apoptosis through evaluating of sub-G1 stage variations [68]. The cells distribution in different phases of cell cycle was determined after treating the MCF-7 cells with IC$_{50}$ concentration of complex **Rh3**, 26.29 μg/mL, for 24 h and the DNA content was detected using flow cytometry in PI-stained cells. After the incubation period, the flow cytometric DNA histogram of **Rh3** showed that the

proportion of cells in the sub-G1 phase of the cell cycle increased significantly ($p = 0.0049$), about 2-fold relative to the control cells (Fig. 8). Comparison of the frequency of treated cell population in other phases with the untreated cells indicates that G1 phase have slightly increased (about 55.47 in treated cells compared to 52.16 in the control group) but the S (about 27.40 in treated cells compared to 31.95 in the control group) and G2 (about 14.78 in treated cells compared to 15.79 in the control group) phases have somewhat decreased (Fig. S26). These results demonstrated that **Rh3** complex as an anti-cancer drug imposed a cytotoxic effect by inducing cell cycle arrest in sub-G1 stage and apoptosis in MCF-7 cells.

### 3.10. Effect of **Rh3** complex on expression of apoptotic pathway genes in MCF-7 cells

The programed cell death, apoptosis, and cell cycle arrest as the gene-regulated phenomena are the crucial aspect of both physiological and pathological processes. Activation of cell cycle arrest and apoptosis are controlled by the proto-oncogenes such as *bcl-2* [69], and tumour suppressor genes such as *p53* [70], and also microRNAs acting as proto-oncogene or tumour suppressor. The proto-oncogene *bcl-2* is involved in the regulation of the mitochondrial pathway of apoptosis [71]. The p53 tumour suppressor protein is a vital regulator in the apoptotic pathway and can efficiently induce apoptosis. The small non-coding RNA molecules or microRNA (miRNA), as a novel class of gene expression regulators, can play a role in tumorigenesis with the regulation of cellular
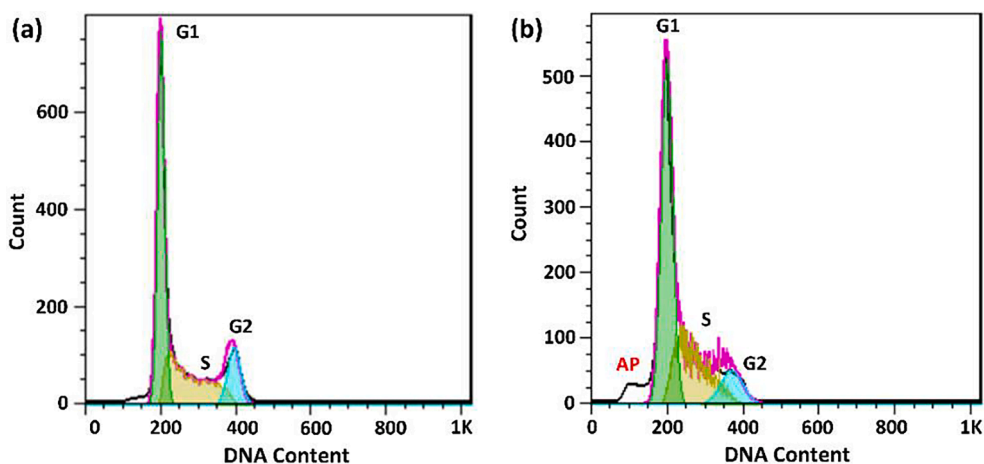


**Fig. 8.** Cell cycle phase distribution of MCF-7 cells (a) untreated and (b) treated with **Rh3** at 26.29 μg/mL (IC$_{50}$) concentration.

processes such as cell proliferation, cell cycle, and apoptotic pathway. These miRNAs control apoptosis by targeting the apoptotic pathway proteins expression. For example, miR-29b, miR-15a and miR-16–1 as the tumour suppressor miRNAs are the pro-apoptotic miRs while miR-21 as the oncomiR is an anti-apoptotic miRNA. Since **Rh3** complex as an anticancer metallodrug promotes apoptosis, its effect was examined on the apoptosis pathway-related genes expression such as *bcl-2*, *p53*, and miR-15a, miR-16–1, miR-21, and miR-29b. After 48 h incubation of MCF-7 cells with the $IC_{50}$ dose of **Rh3**, these cells were analyzed by quantitative real-time polymerase chain reaction (PCR). As evident from the results of real-time PCR analysis (Table 6), the expression of miR-21 and *bcl-2* gene is decreased, and the expression of miR-15a, miR-16–1, miR-29b, and *p53* gene is increased in comparison with the control cells. The statistical data show that the changes in the aforementioned gene expression at the mRNA level are significant except for miR-21 and miR-16–1 (Table 6). *bcl-2* is a direct target of miR-15a and miR-16–1. Presumably, **Rh3** cause the increased miR-15a and miR-16–1 both directly and through negatively regulated *bcl-2* at a post-transcriptional level resulting in apoptosis [72]. Also, the overexpressed miR-29b as a tumour suppressor and repressed expression of miR-21 as a proto-oncogene can induce apoptosis in **Rh3** treated MCF-7 cells via up-regulation of *p53* [73,74]. The higher level of *p53* protein expression, in the treated cells relative to untreated cells, not only lead to the cell apoptosis directly but also through cell cycle arrest. Consequently, the percentage of the apoptotic cells is increased significantly. Taken together, our findings suggest that kinetically inert group 9 complex **Rh3** can be applied as one of the new promising candidates for treating tumour diseases.

### 3.11. Live-cell confocal imaging

Because of the attractive luminescence properties of $d^6$ transition metal complexes as imaging reagents, the interaction of living cells with **qbtz** ligand, as a purely organic molecule, and with cyclometalated **Rh3** complex, for application in live cell imaging, was investigated in detail by a confocal laser-scanning microscope. MCF-7 cells did not show any background fluorescence (Fig. S27). Demonstrations of cell imaging with luminescent Rh(III) complexes, rather than Ir(III) complexes, are extremely rare, with only organometallic Rh(III) complexes available for discussion [9,10,35]. To examine the function of the fluorogenic **Rh3**, as a drug, on the live cells, MCF-7 cells were treated with two different concentrations of the **Rh3** complex at two different incubation times, and compared with the effect of **qbtz** ligand alone. The microscopy images of living MCF-7 cells incubated with **qbtz** at the concentration of 16 μg/mL for 5 h and **Rh3** at the concentrations of 16 and 32 μg/mL for 2 and 5 h, respectively are shown in Fig. 9.

It is clear that both the **qbtz** ligand and **Rh3** complex act as luminescent dyes at 16 μg/mL concentration, indicating their uptake by the live cells. While the **qbtz** ligand with the concentration of 16 μg/mL (75
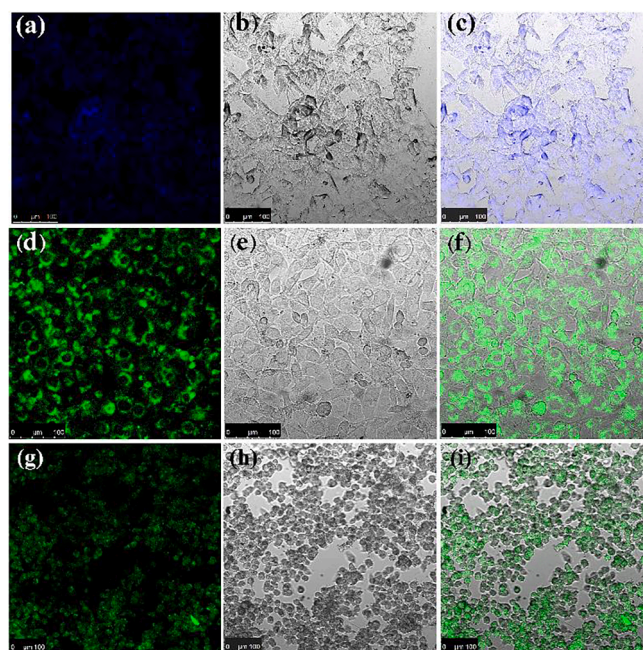


**Fig. 9.** (a, d, g) Confocal phosphorescence images, (b, e, h) bright field images and (c, f, i) their overlay of living MCF-7 cells incubated with **qbtz** at concentration of 16 μg/mL (75 μM) for 5 h and **Rh3** at concentration of 16 μg/mL (19.5 μM) and 32 μg/mL (39 μM) for 2 and 5 h in DMSO and PBS (pH = 7.4, 1:99, v/v) at 37 °C respectively.

μM) and incubation time of 5 h penetrates the cell nucleus (Fig. 9a), **Rh3** complex at the concentration of 16 μg/mL (19.5 μM) for 2 h shows only localization in the perinuclear region without appreciable uptake by the nucleus (Fig. 9d). Based on the MTT assay, the **qbtz** ligand does not show any significant toxicity against MCF-7 cells up to 32 μg/mL (150 μM) despite its penetration in the cell nucleus. However, **Rh3** complex, at the concentration of 32 μg/mL (39 μM) and incubation time of 5 h shows increased cellular uptake efficiency and detrimental effect on MCF-7 cells by penetrating the cell nucleus leading to sever changes in the cell morphology (Fig. 9i) and thus triggering cell death. The remarkable flow cytometry and confocal microscopy results indicate that, **Rh3** with the highest lipophilicity and cytotoxicity is capable of acting as a theranostic agent.

### 4. Conclusion

In summary, we have successfully designed, prepared, and fully characterized three of cyclometalated $[Rh(ppy)_2(N\char`\^N)]^+$ complexes, **Rh1**, **Rh2**, and **Rh3**, with benzothiazole moiety as part of the ancillary N^N ligand for the first time. The photophysical and electrochemical properties of these complexes have been investigated. The **Rh1** and **Rh3** complexes show interesting luminescence properties in DMSO-$H_2O$ (1:1 v/v) at room temperature in the range of visible spectrum. Density functional theory calculations of the lipophilicity indicated that, among the three synthesized Rh(III) complexes, **Rh3** is the best candidate for biological studies. The **Rh3** complex has exhibited proper anticancer activity against MCF-7 cancer cell line, induced cell apoptosis, and caused sub-G1 cell cycle arrest *in vitro*. The effect of **Rh3** complex on the expression of several apoptotic pathway genes in MCF-7 cells was also explored. Apparently, the downregulating of expression of miR-21 and *bcl-2* gene and upregulating the expression of miR-15a, miR-16–1, miR-29b, and *p53* gene, in comparison with the control cells, promote cell apoptosis. Interestingly, flow cytometry and confocal microscopy have proven that the luminescent cationic rhodium(III) complex, **Rh3**, with an emission red-shifted and enhanced relative to its ancillary ligand, **qbtz**, is membrane permeable and acts as a theranostic agent without

**Table 6**
Expression levels of genes in treated MCF-7 cells with **Rh3** compared with control cells (the results are reported as delta cycle threshold). (based on unpaired t-Test statistical method).

| miRNA /Gene | Mean $\Delta ct \pm$ SD in treated cells | Mean $\Delta ct \pm$ SD in control cells | P value | Gene Expression |
|---|---|---|---|---|
| miR-15a | $0.26 \pm 0.1517$ | $1.37 \pm 0.4158$ | 0.0123 | **up-regulation** |
| miR-16–1 | $1.33 \pm 1.3937$ | $2.21 \pm 0.7621$ | 0.3933 | **up-regulation** |
| miR-21 | $5.58 \pm 1.0055$ | $4.60 \pm 0.4331$ | 0.1936 | **down-regulation** |
| miR-29b | $3.59 \pm 0.8816$ | $7.14 \pm 0.1700$ | 0.0024 | **up-regulation** |
| p53 | $9.11 \pm 0.2616$ | $10.32 \pm 0.0318$ | 0.0228 | **up-regulation** |
| bcl-2 | $11.22 \pm 0.0754$ | $10.58 \pm 0.3426$ | 0.0353 | **down-regulation** |

requiring prior membrane permeabilization. Apparently, the unique features of the luminescent Rh(III) complexes will drive continued studies on their development as suitable candidates for diagnostic and therapeutic applications.

## CRediT authorship contribution statement

**Marzieh Sohrabi:** Conceptualization, Investigation, Writing - original draft. **Maryam Bikhof Torbati:** Conceptualization, Investigation, Writing - original draft. **Martin Lutz:** Investigation, Formal analysis, Writing - review & editing. **Soraia Meghdadi:** Conceptualization, Investigation. **Hossein Farrokhpour:** Formal analysis, Software. **Ahmad Amiri:** Investigation, Software. **Mehdi Amirnasr:** Conceptualization, Supervision, Writing - review & editing.

## Declaration of Competing Interest

The authors declare that they have no known competing financial interests or personal relationships that could have appeared to influence the work reported in this paper.

## Acknowledgements

## Appendix A. Supplementary data

Supplementary data to this article can be found online at https://doi.org/10.1016/j.jphotochem.2021.113573.

## References

[1] R.K. Gill, R.K. Rawal, J. Bariwal, Recent advances in the chemistry and biology of benzothiazoles, Arch. Pharm. Chem. Life Sci. 348 (3) (2015) 155–178.

[2] C.G. Hartinger, P.J. Dyson, Bioorganometallic chemistry—from teaching paradigms to medicinal applications, Chem. Soc. Rev. 38 (2) (2009) 391–401.

[3] I. Kitanovic, S. Can, H. Alborzinia, A. Kitanovic, V. Pierroz, A. Leonidova, A. Pinto, B. Spingler, S. Ferrari, R. Molteni, A. Steffen, N. Metzler-Nolte, S. Wölfl, G. A. Gasser, A Deadly organometallic luminescent probe: anticancer activity of a Re$^{I}$ bisquinoline complex, Chem. Eur. J. 20 (2014) 2496–2507.

[4] J. Liu, Y.u. Chen, G. Li, P. Zhang, C. Jin, L. Zeng, L. Ji, H. Chao, Ruthenium(II) polypyridyl complexes as mitochondria-targeted two-photon photodynamic anticancer agents, Biomaterials 56 (2015) 140–153.

[5] W. Sun, Y. Wen, R. Thiramanas, M. Chen, J. Han, N. Gong, M. Wagner, S. Jiang, M. S. Meijer, S. Bonnet, H.-J. Butt, V. Mailänder, X.-J. Liang, S. Wu, Red-light-controlled release of drug–Ru complex conjugates from metallopolymer micelles for phototherapy in hypoxic tumour environments, Adv. Funct. Mater. 28 (2018) 1804227, https://doi.org/10.1002/adfm.201804227.

[6] X.-Q. Zhou, M. Xiao, V. Ramu, J. Hilgendorf, X. Li, P. Papadopoulou, M.A. Siegler, A. Kros, W. Sun, S. Bonnet, The self-assembly of a cyclometalated palladium photosensitizer into protein-stabilized nanorods triggers drug uptake *in vitro* and *in vivo*, J. Am. Chem. Soc. 142 (23) (2020) 10383–10399.

[7] E. Merkul, J.A. Muns, N.J. Sijbrandi, H.-J. Houthoff, B. Nijmeijer, G. Rheenen, J. Reedijk, G.A.M.S. Dongen, An efficient conjugation approach for coupling drugs to native antibodies via the Pt$^{II}$ linker Lx for improved manufacturability of antibody–drug conjugates, Angew. Chem. Int. Ed. 60 (6) (2021) 3008–3015.

[8] X.-D. Song, B.-B. Chen, S.-F. He, N.-L. Pan, J.-X. Liao, J.-X. Chen, G.-H. Wang, J. Sun, Guanidine-modified cyclometalated iridium(III) complexes for mitochondria-targeted imaging and photodynamic therapy, Eur. J. Med. Chem. 179 (2019) 26–37.

[9] M.P. Coogan, V. Fernández-Moreira, Progress with, and prospects for, metal complexes in cell imaging, Chem. Commun. 50 (4) (2014) 384–399.

[10] S.-K. Leung, K.Y. Kwok, K.Y. Zhang, K.-W. Lo, Design of luminescent biotinylation reagents derived from cyclometalated iridium(III) and rhodium(III) bis (pyridylbenzaldehyde) complexes, Inorg. Chem. 49 (11) (2010) 4984–4995.

[11] G.S. Yellol, A. Donaire, J.G. Yellol, V. Vasylyeva, C. Janiak, J. Ruiz, On the antitumor properties of novel cyclometalated benzimidazole Ru(II), Ir(III) and Rh (III) complexes, Chem. Commun. 49 (98) (2013) 11533–11535, https://doi.org/10.1039/c3cc46239k.

[12] H.-J. Zhong, K.-H. Leung, L.-J. Liu, L. Lu, D.-H. Chan, C.-H. Leung, D.-L. Ma, Antagonism of mTOR activity by a kinetically inert rhodium(III) complex, ChemPlusChem. 79 (4) (2014) 508–511.

[13] H.-J. Zhong, H. Yang, D.S.-H. Chan, C.-H. Leung, H.-M. Wang, D.-L. Ma, A metal-based inhibitor of NEDD8-activating enzyme, PloS ONE. 7 (2012) e49574, 2012. Doi: 10.1371/journal.pone.0049574.

[14] J. Weynand, H. Bonnet, F. Loiseau, J.-L. Ravanat, J. Dejeu, E. Defrancq, B. Elias, Targeting G-rich DNA structures with photo-reactive bis-cyclometalated iridium (III) complexes, Chem. Eur. J. 25 (2019) 12730–12739.

[15] Z.-q. Chen, Z.-Q. Bian, C.-H. Huang, Functional Ir$^{III}$ complexes and their applications, Adv. Mater. 22 (13) (2010) 1534–1539.

[16] D. Chao, S. Ni, Highly selective sensing of ClO$_4$ in water with a simple cationic iridium(III) complex and its application in bioimaging, J. Photochem. Photobiol. A: Chem. 324 (2016) 1–7.

[17] Y. You, S.Y. Park, Phosphorescent iridium(III) complexes: toward high phosphorescence quantum efficiency through ligand control, Dalton Trans. 8 (2009) 1267–1282.

[18] C. Ulbricht, B. Beyer, C. Friebe, A. Winter, U.S. Schubert, Recent developments in the application of phosphorescent iridium(III) complex systems, Adv. Mater. 21 (44) (2009) 4418–4441.

[19] W. Tan, Q. Zhang, J. Zhang, H.e. Tian, Near-Infrared photochromic diarylethene iridium(III) complex, Org. Lett. 11 (1) (2009) 161–164.

[20] E. Baggaley, J.A. Weinstein, J.A.G. Williams, Lighting the way to see inside the live cell with luminescent transition metal complexes, Coord. Chem. Rev. 256 (15-16) (2012) 1762–1785.

[21] H. Yersin, A.F. Rausch, R. Czerwieniec, T. Hofbeck, T. Fischer, The triplet state of organo-transition metal compounds. Triplet harvesting and singlet harvesting for efficient OLEDs, Coord. Chem. Rev. 255 (21-22) (2011) 2622–2652.

[22] Q. Zhao, C. Huang, F. Li, Phosphorescent heavy-metal complexes for bioimaging, Chem. Soc. Rev. 40 (5) (2011) 2508–2524, https://doi.org/10.1039/c0cs00114g.

[23] C. Lentz, L. Marcélis, L. Troian-Gautier, K. Robeyns, E. Cauët, B. Elias, Excited-state behavior and photoinduced electron transfer of pH-sensitive Ir(III) complexes with cyclometallation (C/N–) ratios between 0/6 and 3/3, J. Photochem. Photobiol. A: Chem. 405 (2021) 112957, https://doi.org/10.1016/j.jphotochem.2020.112957.

[24] AnnaRita Ghezzi, M. Aceto, C. Cassino, E. Gabano, D. Osella, Uptake of antitumor platinum(II)-complexes by cancer cells, assayed by inductively coupled plasma mass spectrometry (ICP-MS), J. Inorg. Biochem. 98 (1) (2004) 73–78.

[25] P.-K. Lee, H.-W. Liu, S.-M. Yiu, M.-W. Louie, K.-K.-W. Lo, Luminescent cyclometalated iridium(III) bis(quinolylbenzaldehyde) diimine complexes—synthesis, photophysics, electrochemistry, protein cross-linking properties, cytotoxicity and cellular uptake, Dalton Trans. 40 (2011) 2180–2189.

[26] X. Liu, H. Hao, X. Ge, X. He, Y. Liu, Y. Wang, H. Wang, M. Shao, Z. Jing, L. Tian, Z. Liu, Triphenylamine-appended cyclometallated iridium(III) complexes: Preparation, photophysical properties and application in biology/luminescence imaging, J. Inorg. Biochem. 199 (2019) 110757, https://doi.org/10.1016/j.jinorgbio.2019.110757.

[27] S.-P.-Y. Li, J. Shum, K.-K.-W. Lo, Iridium(III) polypyridine complexes with a disulfide linker as biological sensors and cytotoxic agents, Dalton Trans. 48 (2019) 9692–9702.

[28] L.-C. Lee, A.-Y. Tsang, H.-W. Liu, K.-W. Lo, Photofunctional cyclometalated iridium (III) polypyridine complexes bearing a perfluorobiphenyl moiety for bioconjugation, bioimaging, and phototherapeutic applications, Inorg. Chem. 59 (20) (2020) 14796–14806.

[29] Y. Gu, H. Wen, L. Bai, Y.i. Zhou, H. Zhang, L.i. Tian, Y. Zhang, J. Hao, Y. Liu, Exploring anticancer efficiency of mitochondria-targeted cyclometalated iridium (III) complexes, J. Inorg. Biochem. 212 (2020) 111215, https://doi.org/10.1016/j.jinorgbio.2020.111215.

[30] L. Bai, W.-D. Fei, Y.-Y. Gu, H. He, F. Du, W.-Y. Zhang, L.-L. Yang, Y.-J. Liu, Liposomes encapsulated iridium(III) polypyridyl complexes enhance anticancer activity in vitro and in vivo, J. Inorg. Biochem. 205 (2020), 111014, https://doi.org/10.1016/j.jinorgbio.2020.111014.

[31] C.-N. Ko, G. Li, C.-H. Leung, D.-L. Ma, Dual function luminescent transition metal complexes for cancer theranostics: The combination of diagnosis and therapy, Coord. Chem. Rev. 381 (2019) 79–103.

[32] G. Valenti, E. Rampazzo, S. Kesarkar, D. Genovese, A. Fiorani, A. Zanut, F. Palomba, M. Marcaccio, F. Paolucci, L. Prodi, Electrogenerated chemiluminescence from metal complexes-based nanoparticles for highly sensitive sensors applications, Coord. Chem. Rev. 367 (2018) 65–81.

[33] J.J. Soldevila-Barreda, N. Metzler-Nolte, Intracellular catalysis with selected metal complexes and metallic nanoparticles: Advances toward the development of catalytic metallodrugs, Chem. Rev. 119 (2019) 829–869.

[34] J. Shen, T.W. Rees, L. Ji, H. Chao, Recent advances in ruthenium(II) and iridium (III) complexes containing nanosystems for cancer treatment and bioimaging, Coord. Chem. Rev. 443 (2021) 214016, https://doi.org/10.1016/j.ccr.2021.214016.

[35] L.F. Gildea, A.S. Batsanov, J.A.G. Williams, Bright orange/red-emitting rhodium (III) and iridium(III) complexes: tridentate N^C^N-cyclometallating ligands lead to high luminescence efficiencies, Dalton Trans. 42 (2013) 10388–10393.

[36] P. Didier, I. Ortmans, A. Kirsch-De Mesmaeker, R.J. Watts, Electrochemistry and absorption and emission spectroscopy of new orthometalated complexes of rhodium(III) and iridium(III) with the ligands 1,4,5,8-tetraazaphenanthrene and 1,4,5,8,9,12-hexaazatriphenylene, Inorg. Chem. 32 (23) (1993) 5239–5245.

[37] J.B. Waern, C. Desmarets, L.-M. Chamoreau, H. Amouri, A. Barbieri, C. Sabatini, B. Ventura, F. Barigelletti, Luminescent cyclometalated Rh$^{III}$, Ir$^{III}$, and (DIP)$_2$Ru$^{II}$ complexes with carboxylated bipyridyl ligands: synthesis, X-ray molecular structure, and photophysical properties, Inorg. Chem. 47 (2008) 3340–3348.

[38] F. Gärtner, D. Cozzula, S. Losse, A. Boddien, G. Anilkumar, H. Junge, T. Schulz, N. Marquet, A. Spannenberg, S. Gladiali, M. Beller, Synthesis, characterisation and

application of iridium(III) photosensitisers for catalytic water reduction, Chem. Eur. J. 17 (25) (2011) 6998–7006.

[39] C.D. Ertl, C. Momblona, A. Pertegás, J.M. Junquera-Hernández, M.-G. La-Placa, A. Prescimone, E. Ortí, C.E. Housecroft, E.C. Constable, H.J. Bolink, Highly stable red-light-emitting electrochemical cells, J. Am. Chem. Soc. 139 (8) (2017) 3237–3248.

[40] S. Sprouse, K.A. King, P.J. Spellane, R.J. Watts, Photophysical effects of metal-carbon. sigma. bonds in ortho-metalated complexes of iridium(III) and rhodium (III), J. Am. Chem. Soc. 106 (22) (1984) 6647–6653.

[41] S. Meghdadi, M. Amirnasr, P.C. Ford, A robust one-pot synthesis of benzothiazoles from carboxylic acids including examples with hydroxyl and amino substituents, Tetrahedron Lett. 53 (51) (2012) 6950–6953.

[42] N.G. Connelly, W.E. Geiger, Chemical redox agents for organometallic chemistry, Chem. Rev. 96 (2) (1996) 877–910.

[43] M.J. Frisch, G.W. Trucks, H.B. Schlegel, G.E. Scuseria, M.A. Robb, J.R. Cheeseman, G. Scalmani, V. Barone, B. Mennucci, G.A. Petersson, H. Nakatsuji, M. Caricato, X. Li, H.P. Hratchian, A.F. Izmaylov, J. Bloino, G. Zheng, J.L. Sonnenberg, M. Hada, M. Ehara, K. Toyota, R. Fukuda, J. Hasegawa, M. Ishida, T. Nakajima, Y. Honda, O. Kitao, H. Nakai, T. Vreven, J.A. Montgomery, J.E. Peralta, F. Ogliaro, M.J. Bearpark, J. J. Heyd, E. Brothers, K.N. Kudin, V.N. Staroverov, T. Keith, R. Kobayashi, J. Normand, K. Raghavachari, A.P. Rendell, J.C. Burant, S.S. Iyengar, J. Tomasi, M. Cossi, N. Rega, J.M. Millam, M. Klene, J.E. Knox, J.B. Cross, V. Bakken, C. Adamo, J. Jaramillo, R. Gomperts, R.E. Stratmann, O. Yazyev, A.J. Austin, R. Cammi, C. Pomelli, J.W. Ochterski, R.L. Martin, K. Morokuma, V.G. Zakrzewski, G. A. Voth, P. Salvador, J.J. Dannenberg, S. Dapprich, A.D. Daniels, O. Farkas, J.B. Foresman, J.V. Ortiz, J. Cioslowski, D.J. Fox, Gaussian 09, revision D.01; Gaussian, Inc.: Wallingford CT, 2009.

[44] J. Sangster, Octanol-water partition coefficients of simple organic compounds, J. Phys. Chem. Ref. Data 18 (1989) 1111–1227.

[45] R. Mannhold, G.I. Poda, C. Ostermann, I.V. Tetko, Calculation of molecular lipophilicity: State-of-the-art and comparison of log P methods on more than 96,000 compounds, J. Pharm. Sci. 98 (2009) 861–893.

[46] S.C. Rasmussen, M.M. Richter, E. Yi, H. Place, K.J. Brewer, Synthesis and characterization of a series of novel rhodium and iridium complexes containing polypyridyl bridging ligands: potential uses in the development of multimetal catalysts for carbon dioxide reduction, Inorg. Chem. 29 (1990) 3926–3932.

[47] F.O. Garces, R.J. Watts, 1H and $^{13}$C NMR assignments with coordination-induced shift calculations of carbon σ-bonded ortho-metalated rhodium(III) and iridium(III) complexes, Magn. Reson. Chem. 31 (6) (1993) 529–536.

[48] M.T. Indelli, C. Chiorboli, F. Scandola, Photochemistry and photophysics of coordination compounds: Rhodium, Top. Curr. Chem. 280 (2007) 215–255.

[49] G. Calogero, G. Giuffrida, S. Serroni, V. Ricevuto, S. Campagna, Absorption spectra, luminescence properties, and electrochemical behavior of cyclometalated iridium (III) and rhodium(III) complexes with a bis(pyridyl)triazole ligand, Inorg. Chem. 34 (3) (1995) 541–545.

[50] R. Omidyan, M. Iravani, Excited-state intramolecular proton-transfer and photoswitching in hydroxyphenyl-imidazopyridine derivatives: A theoretical study, J. Chem. Phys. 145 (18) (2016) 184303, https://doi.org/10.1063/1.4967199.

[51] A. Amiri, M. Amirnasr, S. Meghdadi, K. Mereiter, V. Ghodsi, A. Gholami, Structural effects on electrochemical properties of the carboxamide complexes [NiII(Mebpb)] and [NiII(Mebqb)], Inorg. Chim. Acta 362 (11) (2009) 3934–3940.

[52] J. Wang, S.L.H. Higgins, B.S.J. Winkel, K.J. Brewer, A new Os, Rh bimetallic with O$_2$ independent DNA cleavage and DNA photobinding with red therapeutic light excitation, Chem. Commun. 47 (35) (2011) 9786–9788, https://doi.org/10.1039/c1cc11562f.

[53] H. Aneetha, P.S. Zacharias, B. Srinivas, G.H. Lee, Y. Wang, Synthesis and characterization of Cp*Rh(III) and Ir(III) polypyridyl complexes: fluxional behaviour of Rh(III) complexes and molecular structure of [Cp*Rh(Ph-terpy)Cl]BF$_4$ complex (Cp* = η5–(C$_5$Me$_5$)), Polyhedron (1999) 299–307.

[54] J.-Y. Lau, P.-K. Lee, K.-K. Tsang, C.-C. Ng, Y.-W. Lam, S.-H. Cheng, K.-W. Lo, Luminescent cyclometalated iridium(III) polypyridine indole complexes—synthesis, photophysics, electrochemistry, protein-binding properties, cytotoxicity, and cellular uptake, Inorg. Chem. 48 (2) (2009) 708–718.

[55] S. Meghdadi, K. Mereiter, M. Amirnasr, F. Karimi, A. Amiri, Synthesis, crystal structure and electrochemistry of cobalt(III) carboxamide complexes with amine and azide ancillary ligands, Polyhedron 68 (2014) 60–69.

[56] S. Meghdadi, M. Amirnasr, K. Mereiter, A. Amiri, V. Ghodsi, Synthesis, characterization and electrochemistry of carboxamido Co(III) complexes: The crystal structure of [CoIII(Mebpb)(N-MeIm)$_2$]BPh$_4$·CH$_3$OH, Inorg. Chim. Acta 363 (2010) 1587–1592.

[57] I. Ortmans, P. Didier, A. Kirsch-De Mesmaeker, New charge transfer luminescent polymetallic complexes of rhodium(III), iridium(III), and ruthenium(II) with the bridging ligand 1,4,5,8,9,12-Hexaazatriphenylene, Inorg. Chem. 34 (14) (1995) 3695–3704.

[58] E. Holder, V. Marin, D. Kozodaev, M.A.R. Meier, B.G.G. Lohmeijer, U.S. Schubert, Iridium(III) complexes with PEO and PS polymer macroligands and light-emitting properties: Synthesis and characterization, Macromol. Chem. Phys. 206 (10) (2005) 989–997.

[59] F. Neve, M.L. Deda, F. Puntoriero, S. Campagna, Ionic luminescent cyclometalated Ir(III) complexes with polypyridine co-ligands, Inorg. Chim. Acta 359 (5) (2006) 1666–1672.

[60] S.P. Oldfield, M.D. Hall, J.A. Platts, Calculation of lipophilicity of a large, diverse dataset of anticancer platinum complexes and the relation to cellular uptake, J. Med. Chem. 50 (21) (2007) 5227–5237.

[61] T. Mosmann, Rapid colorimetric assay for cellular growth and survival: Application to proliferation and cytotoxicity assays, J. Immunol. Methods 65 (1-2) (1983) 55–63.

[62] M.N. Zafar, M. Masood, G.-S. Chaudhry, T.S.T. Muhammad, A.F. Dalebrook, M. F. Nazar, F.P. Malik, E.U. Mughal, L.J. Wright, Synthesis, characterization and anti-cancer properties of water-soluble bis(PYE) pro-ligands and derived palladium(II) complexes, Dalton Trans. 48 (2019) 15408–15418.

[63] S. Dieckmann, R. Riedel, K. Harms, E. Meggers, Pyridocarbazole-rhodium(III) complexes as protein kinase inhibitors, Eur. J. Inorg. Chem. 2012 (5) (2012) 813–821, https://doi.org/10.1002/ejic.v2012.510.1002/ejic.201101175.

[64] C.-H. Leung, H. Yang, V.-Y. Ma, D.-H. Chan, H.-J. Zhong, Y.-W. Li, W.-F. Fong, D.-L. Ma, Inhibition of Janus kinase 2 by cyclometalated rhodium complexes, Med. Chem. Commun. 3 (6) (2012) 696–698, https://doi.org/10.1039/c2md00306f.

[65] N. Adarsh, P.S. Saneesh Babu, R.R. Avirah, M. Viji, A.S. Nair, D. Ramaiah, Aza-BODIPY nanomicelles as versatile agents for in vitro and in vivo singlet oxygen triggered apoptosis of human breast cancer, J. Mater. Chem. B 7 (2019) 2372–2377.

[66] J. Klucar, M. Al-Rubeai, G2 cell cycle arrest and apoptosis are induced in Burkitt's lymphoma cells by the anticancer agent oracin, FEBS Lett. 400 (1997) 127–130.

[67] L. Gamet-Payrastre, P. Li, S. Lumeau, G. Cassar, M.-A. Dupont, S. Chevolleau, N. Gasc, J. Tulliez, F. Tercé, Sulforaphane, a naturally occurring isothiocyanate, induces cell cycle arrest and apoptosis in HT29 human colon cancer cells, Canc. Res. 60 (2000) 1426–1433.

[68] Y. Yuan, J. Wu, B. Li, J. Niu, H. Tan, S. Qiu, 3-D micro-architecture and mechanical response of soil cemented via microbial-induced calcite precipitation, Sci. Rep. 8 (2018) 992–1001.

[69] Y.M. Janumyan, C.G. Sansam, A. Chattopadhyay, N. Cheng, E.L. Soucie, L.Z. Penn, D. Andrews, C.M. Knudson, E. Yang, Bcl-xL/Bcl-2 coordinately regulates apoptosis, cell cycle arrest and cell cycle entry, EMBO J. 22 (2003) 5459–5470.

[70] M.B. Kastan, C.E. Canman, C.J. Leonard, P53, cell cycle control and apoptosis: Implications for cancer, J. Cancer Metastasis Rev. 14 (1) (1995) 3–15.

[71] W.S. Lee, S.M. Yi, J.W. Yun, J.H. Jung, D.H. Kim, H.J. Kim, S.-H. Chang, GonSup Kim, C.H. Ryu, S.C. Shin, S.C. Hong, Y.H. Choi, J.-M. Jung, Polyphenols isolated from Allium cepa L. induces apoptosis by induction of p53 and suppression of Bcl-2 through inhibiting PI3K/Akt signaling pathway in AGS human cancer cells, J Cancer Prev. 19 (1) (2014) 14–22.

[72] A. Cimmino, G.A. Calin, M. Fabbri, M.V. Iorio, M. Ferracin, M. Shimizu, S. E. Wojcik, R.I. Aqeilan, S. Zupo, M. Dono, L. Rassenti, H. Alder, S. Volinia, C.-g. Liu, T.J. Kipps, M. Negrini, C.M. Croce, miR-15 and miR-16 induce apoptosis by targeting BCL2, PNAS 102 (39) (2005) 13944–13949.

[73] Y. Liu, X. Lu, Non-coding RNAs in DNA damage response, Am. J. Cancer Res. 2 (2012) 658–675.

[74] X. Ma, S.N. Choudhury, X. Hua, Z. Dai, Y. Li, Interaction of the oncogenic miR-21 microRNA and the p53 tumor suppressor pathway, Carcinogenesis 34 (2013) 1216–1223.